Monthly Notices
of the Royal Astronomical Society

Grain Alignment at High Extinctions in the Southern Coalsack, Probed with Spectro-polarimetry

Journal:	*Monthly Notices of the Royal Astronomical Society*
Manuscript ID	MN-24-0434-MJ.R1
Manuscript type:	Main Journal
Date Submitted by the Author:	10-May-2024
Complete List of Authors:	Andersson, B-G; Boston College, Institute for Scientific Research; Universities Space Research Association, SOFIA Science Center Minter, Avery; Santa Clara University, Department of Physics Maharana, Siddharth; South African Astronomical Observatory Potter, Stephen; South African Astronomical Observatory; University of Johannesburg, Department of Physics Singh, Saikhom ; Indian Institute of Astrophysics Soam, Archana; Indian Institute of Astrophysics Kulas, Kristin; Santa Clara University, Department of Physica Jones, Terry; University of Minnesota, Minnesota Institute for Astrophysics
Keywords:	(ISM:) dust, extinction < Interstellar Medium (ISM), Nebulae, polarization < Physical Data and Processes

MNRAS 000, 1–16 (2023) Preprint 10 May 2024 Compiled using MNRAS LATEX style file v3.0

Grain Alignment at High Extinctions in the Southern Coalsack, Probed with Spectro-polarimetry

B-G Andersson,[1]★ Avery Minter,[2] Siddharth Maharana,[3] Stephen B. Potter,[3,5] Saikhom Pravash Singh,[4] Archana Soam,[4] Kristin R. Kulas,[2] Terry J. Jones,[6]

[1]*Visiting Scholar, Institute for Scientific Research, Boston College, Kenny Cottle Hall 217, 885 Centre St., Newton, MA 02459*
[2]*Department of Physics, Santa Clara University, Sobrato Campus for Discovery and Innovation, 500 El Camino Real, Santa Clara, CA 95053, USA*
[3]*South African Astronomical Observatory, PO Box 9, Observatory Rd., 7935 Observatory, South Africa*
[4]*Indian Institute of Astrophysics, II Block, Koramangala, Bengaluru 560034, India*
[5]*Department of Physics, University of Johannesburg, PO Box 524, Auckland Park 2006, South Africa*
[6]*Minnesota Institute for Astrophysics, University of Minnesota, 116 Church Street Se, Minneapolis, MN 55455 , USA*

Accepted XXX. Received YYY; in original form ZZZ

ABSTRACT

The size distribution of interstellar dust grains is important to the evolution of the interstellar medium and proto-planetary disk dynamics. Because the optical-to-near-infrared polarization spectrum is sensitive to the size distribution of aligned grains and the spectral energy distribution of the radiation, it can probe the grain size distribution in molecular clouds. We present a study of the starless Southern Coalsack cloud, based on multi-wavelength polarimetry of background stars with extinctions up to 10 mag. We find that for $A_V \gtrsim 3$ mag, the location of the polarization peak ($\lambda_{max}(A_V)$) bifurcates, mirroring the behaviour seen in the Taurus molecular cloud. We use the Stokes-I spectra of the high-extinction stars to establish spectral classifications, and archival photometry to derive total-to-selective extinctions, R_V, for the lines of sight. We find that the bifurcation in $\lambda_{max}(A_V)$ is **not** associated with a bifurcation in R_V. ***Ab initio* RAT modeling requires some grains significantly above the size cut-off in diffuse gas ($a_{max} \sim 0.3\mu m$) to reproduce the large λ_{max} values on the $\lambda_{max}(A_V)$ "upper branch". Without additional grain growth, the bifurcation implies a very large density contrast between clump and inter-clump gas.** A steep negative slope in $p/A_V(A_V)$ for the high extinction stars, together with an additional, marked, deficiency in p/A_V for the lines of sight at the top of the upper branch, implies an upper cut-off in the total grain size distribution of a_{max} ~0.4-0.5 μm, even in at $A_V > 5$ mag.

Key words: (ISM:) dust, extinction – polarization – ISM: individual objects: Southern Coalsack

1 INTRODUCTION

Grain growth in the interstellar medium (ISM) has important implications for the heating, cooling and chemistry of the medium. In addition, extending the upper grain size distribution beyond the Mathis et al. (1977, "MRN") diffuse ISM cut-off at $a_{max} \approx 0.3$ μm (where a is the effective grain radius) has significant effects on the angular momentum shedding and evolution of young protostellar disks, and planet formation (e.g. Marchand et al. 2020; Lebreuilly et al. 2020). Where, when, and how, grain growth is initiated, however, is poorly constrained in molecular clouds.

Dust grains are thought to grow through coagulation in dense gas (e.g. Ossenkopf 1993; Ormel et al. 2009), but limited observational evidence exists to constrain the process (cf Whittet et al. 2001; Shenoy 2003; Boogert et al. 2015). While grain growth is expected to happen, for a uniform cloud contracting on free-fall time scales, even at a gas density of 10^5 cm^{-3}, the process should not have time to proceed in the lifetime of the cloud (Ormel et al. 2009). Evidence for grain coagulation in moderate density gas has, however, been reported by Ysard et al. (2013), who found that near-and far-infrared (NIR/FIR) observations toward the Taurus molecular cloud indicate significant grain growth at densities above 10^3 cm^{-3}. The uncertain emissivities and temperatures of the dust on the line of sight, however, make these infrared (IR) based photometric results model dependent. Independent probes of the grain sizes are needed to confirm and calibrate such data. For small opacities, the [UV]-optical-IR extinction curve can be used, but at large opacities, the pair-method (e.g. Whittet 2003) becomes unviable.

In our previous paper (Vaillancourt et al. 2020, hereafter V20) we used spectro-polarimetry of stars background to the Taurus molecular cloud, a low-mass star forming cloud, to show that grain growth is **likely** required to reproduce the observations on some lines of sight (l.o.s.) at extinctions beyond that characteristic of ice formation (A_V ~3-4 mag). Here we extend this study to the starless Southern Coalsack cloud.

Multiband optical/near infrared (O/NIR) polarimetry provides a direct means to probe the dust size distribution of aligned grains (Andersson et al. 2015, hereafter ALV15), and to e.g. find the best sources for JWST dust spectroscopy **targeting grain growth** (e.g.

★ E-mail: astrobgandersson@gmail.com

Paladini et al. 2021). The location (λ_{max}) of the peak (p_{max}) of the ISM optical polarization - "Serkowski" – curve (Serkowski 1973):

$$p(\lambda) = p_{max} \cdot exp\{-K \cdot ln^2(\frac{\lambda}{\lambda_{max}})\} \quad (1)$$

is set by the size distribution of **aligned** grains along the l.o.s. (Kim & Martin 1995; Clayton et al. 2003). The K parameter encodes the width of the curve, and is generally correlated with λ_{max} (Wilking et al. 1982; Whittet 1992).

In addition to the dichroic extinction responsible for the shape of the Serkowski curve (e.g Kim & Martin 1995), scattering off of small grains or polarizable molecules, in the astronomical sources or the Earth's atmosphere, can give rise to Rayleigh scattering with the functional form:

$$R(\lambda) = c \cdot \lambda^{-4} \quad (2)$$

While such scattering has been observed, e.g. in reflection nebulae or circumstellar material (e.g. Kastner & Weintraub 1994; Andersson & Wannier 1997; Olofsson et al. 2012; Andersson et al. 2013), the gas and dust on the lines of sight discussed here are not close to bright stars, and we would therefore not expect astronomical Rayleigh scattering to be present. As we will discuss below, atmospheric Rayleigh scattering may however be an issue.

An additional advantage of using the spectral shape of the **dichroic** polarization, **rather than the absolute level of polarization**, is that it is, to a high degree, insensitive to depolarization effect due to multiple components of, and turbulence in, the magnetic field. **Because polarization is a differential effect, the strong wavelength dependence of the extinction does not translate to the polarization. Also, even though non-parallel magnetic fields on the l.o.s. can lower the total level of polarization, it does not affect the wavelength dependence. This can be seen by the lack of wavelength dependence of the position angle θ in Eqs. A5 and A6 in Jones (1989), where θ represents the magnetic field geometry (only). Any addition of a wavelength dependence for θ would have to derive from the physics of the alignment mechanism, not turbulence in the magnetic field. As discussed by e.g. Jones et al. (1992) the slope of the polarization efficiency ($p/A_V(A_V)$) can provide statistical information about the magnetic field turbulence which we will use in our analysis (e.g. Sec. 4.2)**

A universal, linear, λ_{max} relationship exists in the ISM at A_V <4 mag. (Whittet et al. 2001; Andersson & Potter 2007, hereafter AP07). AP07 further found that the intercept of the $\lambda_{max}(A_V)$ relationship was linearly dependent on the average of the total-to-selective extinction (R_V) for each of the six clouds in their study.

These results can be understood under the modern "radiative alignment torque" (RAT) paradigm (Lazarian & Hoang 2007, hereafter LH07; ALV15) for interstellar grain alignment, as due to the reddening of the radiation field to the clouds, for a fixed grain size distribution, which can vary between clouds (as traced by **the average R_V in each cloud**).

RAT alignment predicts that - to first order - a paramagnetic (silicate) dust grain will align if exposed to an anisotropic radiation field with wavelengths less than the grain diameter: $\lambda < 2a$ (e.g. LH07). Together with the well-established power-law distribution of ISM dust grain sizes (Mathis et al. 1977, "MRN") this condition explains the shape of the ISM polarization curve. As shown by Kim & Martin (1995) the polarization curve for low extinction l.o.s requires a lower size limit of the *aligned* grains of d~0.09μm (or ~900Å) - i.e. the Lyman limit for the interstellar radiation field. The dependence on the extinction (Whittet et al. 2001; Andersson & Potter 2007), can be understood as due to the further loss of the bluest radiation (beyond the Lyman limit) as the radiation field is reddened into the cloud.

As discussed by AP07, the geometry of the cloud, radiation field, and line of sight can complicate this empirical relationship. If the line of sight extinction is not a good approximation of the effective opacity - that seen by a grain towards the external radiation field - the observed polarization curve, and specifically λ_{max}, will deviate from the general trend (cf Figure 7 of AP07). To identify such lines of sight, AP07 used a comparison of the far infrared (FIR) I(60μm)/I(100μm) ratio with the observed visual extinction, assuming that the I(60μm)/I(100μm) ratio reflects the dust temperature, governed by radiative heating. For five of the clouds studied in AP07, clear anti-correlations are found for the field-star samples between the I(60μm)/I(100μm) ratio and A_V, with a few outliers for each cloud. For the Southern Coalsack this procedure did, however, not yield a statistically significant correlation, possibly due to the strong influence of diffuse background sources in the FIR data. In AP07, based on the similarity of the I(60μm)/I(100μm) vs. A_V data distribution for the Chamaeleon and Taurus clouds, on the one hand, and that for the Southern Coalsack, **on the other,** the functional relationships for Chamaeleon and Taurus were used to identify possible outlier points in the Coalsack.

The radiative grain alignment driving is balanced by grain spin randomization, dominated by gas-grain collisions, dependent on the collision rate $r \propto n_{gas} \cdot \sqrt{T_{gas}}$ (Draine & Lazarian 1998). If, as is commonly assumed, the timescale for collisional disalignment is given by the time it takes for a grain to collide with its own mass in gas particles, it is easy to show that this timescale $\tau_{gas} \propto a$; i.e. the smallest grains are most easily disaligned.

For high enough gas densities and temperatures (at a give extinction), gas-grain collisions can then determine the smallest aligned grain size: a_{min}^{align} which can also cause deviations from the general $\lambda_{max}(A_V)$ relationship.

In a study of the Taurus molecular cloud, including deep l.o.s., V20 found that, for part of the sample, the low-A_V $\lambda_{max}(A_V)$ relation is still valid to A_V ≥10 mag. (Figure 4 "Lower Branch"). A much steeper relationship is found for the remaining sample, beyond, A_V >4 mag. (Figure 4 "Upper Branch"). RAT based *ab initio* modeling closely matches these results. The "lower branch" is well fit with a standard, fixed, MRN grain size distribution, with a maximum grain size of a_{max} ~0.3μm, exposed to a reddened radiation field and a constant gas density and temperature. For the lowest A_V l.o.s. the modeling indicate that gas-dust collisions at n~1-10×10^3 cm^{-3} determine a_{min}^{align} (cf. V20, Figure 5). The upper branch was best modeled with a combination of enhanced collisional disalignment of small grains (gas densities of about n~4×10^4 cm^{-3}) and grain growth, with the largest grains being at least twice the size of those for the lower branch. It is noteworthy that, at least for the Taurus cloud, the phase space between the two branches is effectively empty. This may reflect that the clump-in-clump density contrast in the dense gas is high, such that the polarization from a clump fully dominates that from any inter-clump material on a given line of sight. For the high-extinction targets, B-band photometry was not available, and therefore also not R_V.

Finally, a group of targets at A_V ≈2 mag showed enhanced values of λ_{max} but "normal" values of R_V (~3.1). These likely correspond to enhanced gas density, without grain growth. As noted by V20, the bifurcation point of the two "branches" is consistent with the extinction where H_2O and CO_2 ices first appear between A_V=3 and 4 mag. (Boogert et al. 2015).

These results, therefore, indicated a clumpy cloud medium where the "lower branch" probes the inter-clump gas, with a standard MRN grain size distribution, while the "upper branch" probes dense regions where grain growth has taken place, beyond the ISM size distribution. The bifurcation points to grain growth that requires both an enhanced density and the presence of ice mantles to mediate the coagulation process (Ormel et al. 2009). For extinctions below the onset of ice mantle formation, these results indicate that enhanced gas density in clumps leads to localized, moderate, enhancement in λ_{max}, providing a new probe of the gas density structure in moderate density molecular clouds.

In this paper, we present a parallel study of the star-less Southern Coalsack cloud, aimed at testing whether the "two branch" structure is present in clouds beyond the Taurus molecular cloud. As will be discussed below, our present results find the bifurcation also in the Coalsack. However, while requiring, and supporting, general grain growth, they do not support the triggering of that grain growth by ice mantle formation.

1.1 The Southern Coalsack

The Southern Coalsack is an ideal object for our study, because of the characteristics of the cloud and the many available supporting datasets. The cloud is nearby (d~180pc), well studied, located close to the Galactic plane, and reaches maximum extinctions of $A_V \geq 15$ mag (Jones et al. 1984, hereafter JHB84). It contains dense molecular cores, but no signs of star formation, although recent observations and simulations imply that it may be in the initial stage of collapse due to the passage of the shell of the Upper Centaurus Lupus superbubble (Andersson et al. 2004; Lada et al. 2004; Hennebelle et al. 2006). The cloud has been very well studied from X-ray to radio, and in photometry, [molecular] line spectroscopy, and polarization (e.g. JHB84, Nyman et al. 1989; Duncan et al. 1997; Walker & Zealey 1998; Andersson et al. 2004, AP07). For a more complete review, see Nyman (2008).

As discussed by Andersson et al. (2004), the molecular cloud is surrounded by hot gas giving rise to the formation of the O^{5+} ion, seen as far-ultraviolet [O VI] absorption, and generating soft X-ray emission. Based on a combination of a Davis-Chandrasekhar-Fermi analysis and a simplified polarization radiative transfer, Andersson & Potter (2005) found that the magnetic field in the Coalsack envelope is very strong ($B_\perp \approx 90\mu$G), and therefore in rough equipartition with the X-ray emitting gas. Duncan et al. (1997) found polarized 2.4 GHz [synchrotron] emission along the SE and NW rims of the dense cloud, where the magnetic field (based on optical polarization data, e.g. Andersson & Potter (2005)) is oriented parallel to the projected cloud surface. These results, together with the findings of de Geus (1992), Crawford (1995), and Lada et al. (2004), can be understood as resulting from the expansion of the Upper Centaurus-Lupus superbubble, with its shell overtaking, enveloping, and compressing the Southern Coalsack about 1 Myr ago.

2 OBSERVATIONS AND DATA REDUCTION

In order to efficiently probe the grain alignment over a broad range of extinction, we observed 52 low-extinction ($A_V \leq 3$ mag) stars (and one star at A_V=3.5 mag) with the 1.9m telescope at the South African Astronomical Observatory (SAAO) using the HIPPO photo-polarimeter in the five Johnson-Cousins filters, and 7 stars at high extinction ($A_V \geq 4$ mag) using the Robert Stobie Spectrograph (RSS) with grism PG300 covering 4650 - 9960 Å, in polarimetry mode, on the South Africa Large Telescope (SALT).

To use a consistent set of stellar and extinction parameters, we extracted spectral classes for the HIPPO targets from the "ATLAS" survey (Skiff 2014), and selected the luminosity classification from the Michigan Spectral Survey (Houk & Cowley 1975), where available. For CPD-64 1976 we used the classification from Seidensticker (1989). We extracted photometry from the Tycho (Høg et al. 2000) and 2MASS (Cutri et al. 2003) surveys (all through the Vizier service at CDS, U. Strasbourg) and calculated total-to-selective and visual extinctions using the intrinsic colours from Fitzgerald (1970) and Ducati et al. (2001), as compiled by Neill Reid (https://www.stsci.edu/ inr/intrins.html). For the total-to-selective extinction, R_V, we used the expression derived by Whittet & van Breda (1978)

$$R_V = 1.1 \cdot \frac{E_{V-K}}{E_{B-V}} \quad (3)$$

Target data are listed in Table 1.

The SALT/RSS targets (Table 2) are taken from the NIR photometric and H-band polarimetry surveys of Jones et al. (1980, "JHR80") and Jones et al. (1984, "JHB84"). For the high extinction targets, in addition to the above methods we also derived R_V values using fits of the extinction over the optical and NIR range (see below). Detailed target information for this set will be discussed below.

In addition, we will in our analysis utilize the earlier 1.9m/HIPPO observations of the Coalsack, presented in Andersson & Potter (2007) [1].

2.1 1.9m/HIPPO

We used the HIPPO photo-polarimeter (Cropper 1985; Potter et al. 2008), mounted to the 1.9 m telescope at the SAAO, using Johnson-Cousins filters ($UBVR_CI_C$; λ_{eff}=0.36, 0.44, 0.55, 0.64, 0.79 μm), on the nights of 2021 May 4-10. HIPPO was configured in its simultaneous linear and circular polarimetry mode (no circular polarization was detected in any target). A RCA31034A GaAs photomultiplier was used as the detector. In addition to our science targets, the high-polarization (HD 110984, HD 298383, HD 147084, HD 154445, HD 160529) and zero-polarization standards (HD 94851, HD 176425) stars were observed during the campaign. Sky polarization corrections were accomplished by sky observations immediately prior to, and following, the main observation. The data were reduced using the well-tested custom software package (Cropper 1985).

The reduced data are presented in Table 3.

2.2 SALT/RSS

High-extinction stars, selected from JHB84, were observed in service mode with the South Africa Large Telescope (SALT; O'Donoghue et al. 2006), using the Robert Stobie Spectrograph (RSS) in long-slit spectropolarimetry mode (Potter et al. 2016).

SALT is an Alt-Az mounted telescope, which has a fixed altitude and can move freely in the azimuth direction. The RSS is located at the prime focus on a moving platform, enabling tracking a source

[1] We note that due to a typographical error, the Serkowski values for HD 110245 are misquoted in Table 3 of that paper. The correct values are: p_{max}=1.22±0.02%; λ_{max}=0.51±0.02 μm). The polarization data for the star in Table 2 of that paper are correct.

Table 1. 1.9m/Hippo Targets

Star	RA (2000) [hh:mm:ss]	Dec (2000) [dd:mm:ss]	Sp.	V [mag]	R_V	A_V [mag]	d[a] [pc]
CPD-64 1900	12:25:01.01	-65:05:17.9	B8	9.93	4.61±0.92	1.14±0.31	1575±46
HD 108417	12:27:46.46	-63:53:04.8	A1 V	8.98	4.42[b]	0.58±0.19	275±1
HD 108418	12:27:46.46	-64:34:39.1	B5V:n(e)	8.43	6.07±0.64	2.03±0.29	1409±33
HD 108804	12:30:31.31	-61:49:04.4	F2 V	8.42	4.42[b]	<0.24	220±1
HD 109065	12:32:17.17	-61:43:42.5	A1 Vn	8.16	4.42[b]	0.46±0.17	590±162
CPD-64 1975	12:38:53.53	-65:08:17.7	B5/7	10.69	4.18±0.48	2.96±0.47	295±33
HD 109891	12:39:01.01	-62:31:45.9	A0 V	8.73	4.42[b]	0.92±0.32	312±7
HD 109937	12:39:19.19	-63:21:41.2	B2/3III	9.37	3.69±0.24	2.09±0.17	1432±24
CPD-64 1976	12:39:36.36	-65:08:47.6	A0 V	10.90	4.52±0.76	2.33±0.54	367±11
HD 110102	12:40:28.28	-63:16:59.7	B9:	10.15	3.23±0.39	2.02±0.29	242±8
HD 110151	12:40:42.42	-60:54:47.2	B9.5 IV	8.72	4.42[b]	0.65±0.26	630±17
HD 110245	12:41:34.34	-66:58:12.6	F8/G0 III + A3:	8.40	4.42[b]	0.36±0.20	446±13
HD 110432	12:42:50.50	-63:03:31.1	B0.5 IVep	5.31	5.58±0.82	2.49±0.39	438±15
HD 110433	12:42:52.52	-63:11:07.1	B2/3 IV/V	9.06	4.19±0.33	1.78±0.18	1491±129
HD 110498	12:43:15.15	-61:38:56.2	B0.5 III	9.73	3.85±0.21	2.55±0.19	1987±51
HD 110660	12:44:26.26	-64:03:19.0	B3/5	9.99	3.98±0.31	2.53±0.27	1819±38
HD 110715	12:44:49.49	-64:57:51.7	B9 V	8.71	4.69±0.67	1.71±0.29	525±9
HD 110737[c]	12:44:57.57	-65:19:09.4	B9.5 V	8.54	4.72±0.76	1.66±0.36	141±18
HD 110946	12:46:29.29	-64:55:03.6	B1 III	9.24	4.40±0.30	1.99±0.19	2110±54
HD 110984	12:46:45.45	-61:11:11.5	B1 II/III	9.01	4.07±0.21	2.41±0.17	1739±177
HD 111024	12:47:07.07	-63:05:08.2	B5 III	9.00	4.00±0.36	1.48±0.17	671±12
CPD-64 2006	12:47:09.09	-65:39:03.1	B1.5 V	10.16	4.42[b]	1.19±0.35	2644±122
HD 111174	12:48:10.10	-63:02:19.3	A3 V	8.14	5.62±1.10	1.30±0.35	234±1
HD 111237	12:48:45.45	-64:45:55.3	B8 V	10.25	5.03±0.81	1.72±0.39	1113±38
HD 111303	12:49:07.07	-61:04:00.3	F0 IV	9.08	4.42[b]	0.63±0.17	366±2
HD 111343	12:49:27.27	-64:12:10.1	A2 III	9.30	4.70±0.31	3.02±0.27	2459±78
HD 111688	12:51:59.59	-63:08:31.9	B8/9 II/III	9.95	4.04±0.42	2.38±0.33	981±13
HD 111779	12:52:35.35	-63:03:13.5	B5/7 V	9.71	4.30±0.46	2.10±0.31	788±7
HD 111827	12:52:50.50	-64:49:00.9	B5 III	8.35	4.87±0.50	1.44±0.20	742±11
HD 111992	12:54:07.07	-63:09:58.6	A1 V	8.88	4.27±0.35	2.08±0.23	313±41
HD 112225[c]	12:55:57.57	-60:54:59.3	A8 V	8.44	4.42[b]	<0.24	175±1
HD 112295	12:56:33.33	-61:20:07.0	B8/9 II/III	9.50	3.63±0.31	2.43±0.27	461±43
HD 112637	12:59:16.16	-63:18:16.1	B2 III	9.56	3.68±0.35	2.05±0.26	1224±20
HD 112661	12:59:21.21	-62:17:20.6	B0/1 III/IV	9.28	4.09±0.17	3.20±0.18	4200±2800
HD 112785	13:00:10.10	-62:25:01.4	B3/5	9.77	4.66±0.38	2.44±0.28	2152±171
HD 112954	13:01:23.23	-62:55:30.2	B9 IV	8.39	4.06±0.45	2.04±0.27	383±3
HD 113014	13:01:48.48	-62:10:51.8	B2 III	9.10	4.34±0.43	2.11±0.28	6831±4096
HD 113034	13:01:53.53	-61:49:55.8	B0/1 III:	9.31	3.94±0.12	4.50±0.19	1950±79
HD 113348	13:04:06.06	-61:27:43.7	A9 V	9.18	7.68±1.63	1.12±0.33	436±2
HD 113511	13:05:20.20	-64:03:02.2	B0 IV/V	9.03	3.32±0.18	2.42±0.18	1914±88
HD 113541	13:05:41.41	-63:22:14.5	B8/9 III	9.78	4.29±0.46	2.31±0.33	698±8
HD 113742	13:06:54.54	-61:56:38.1	B1/2 III:	9.21	4.03±0.23	2.21±0.17	837±549
CPD-61 3462	13:07:33.33	-62:22:16.9	B0.5 III	9.20	3.96±0.17	2.89±0.17	1818±49
HD 113968	13:08:26.26	-61:14:38.5	B2/3 IV	8.79	4.70±0.61	1.09±0.19	1101±27
HD 114157	13:10:01.01	-64:33:38.4	A7/8 V	9.21	4.42[b]	<0.56	478±4
HD 114653	13:13:08.08	-63:36:29.9	B8 III	8.62	4.83±0.72	1.24±0.25	568±14
CPD-60 4528	13:13:12.12	-61:05:21.3	B1 III	8.76	3.85±0.26	1.74±0.15	2317±93
HD 114718	13:13:35.35	-63:06:09.9	B9 III/IV	8.43	5.02±1.19	1.05±0.30	548±5
HD 114720	13:13:38.38	-64:09:04.1	B8 V	9.66	4.42[b]	0.78±0.23	591±33
HD 114719	13:13:40.40	-63:41:01.5	A2/3 III	9.47	3.83±0.54	1.25±0.23	307±1

a: Based on Gaia DR2 parallaxes, except for HD 112661 which is taken from Bailer-Jones et al. (2018)
b: For stars with $E_{B-V}/\sigma E_{B-V}$ <5 we have assigned R_V as the average R_V of the rest of the sample
c: These stars have nominal distances foreground to the Coalsack.

during the observation sequence. A consequence of this design is that the polarimetric behaviour of the telescope-instrument combination is a strong function of the position of the source on the sky with respect to the telescope axis during the observations. The polarimetric calibration model for the instrument aims to account for this effect.

All observations were done in scheduling/observing blocks for which observations through ~~with~~ **half-wave plate positions of** 0°, 22.5°, 45° **and** 67.5° **East of North execute consecutively.** This is ~~one of the~~ standard ~~available~~ long-slit polarimetry modes on the RSS. For this work, we employed the PG300 grating, which covers the wavelength range of 4000Å to 1000Å with a spectral resolution of around 17.5Å, suitable for broad-band polarimetry including to constrain the Serkowski

Table 2. SALT/RSS targets

Star	RA (2000) [hh:mm:ss]	Dec (2000) [dd:mm:ss]	BP[a] [mag]	Sp.	T^a_{eff} [K]	A_V [mag]	A^a_0 [mag]	d[a] [kpc]	Offset[b] [″]
[JHR80] D-1	12:31:02.35	-63:47:23.5	16.90±0.01	G4 III	7856	5.9±0.4	6.6±0.20	1.57±0.06	237
[JHR80] D-4	12:31:03.86	-63:40:21.6	16.88±0.01	G0 I	-	10.6±0.4	-	12.4±5.7	315
[JHR80] D-6	12:31:07.43	-63:41:06.0	18.89±0.01	K5 III:	4475	7.6±0.9	9.7±0.06	4.43±0.15	264
[JHR80] D-14	12:31:39.83	-63:47:20.8	18.03±0.01	G9 III	-	7.2±0.3	-	1.72±0.19	169
[JHR80] D-17	12:31:59.22	-63:43:34.3	15.42±0.01	G6 III	-	6.4±0.3	-	0.89±0.12	214
[JHR80] D-19	12:31:59.62	-63:47:25.7	17.49±0.01	G9 III	7908	7.1±0.3	7.89±0.04	1.64±0.08	257
D-19B[c]	12:32:04.91	-63:46:57.2	17.08±0.01	K5 V:	-	2.8±0.9	-	1.72±0.09	271
[JHR80] D-20	12:32:03.99	-63:43:40.5	16.73±0.01	K5 III	-	5.4±0.5	-	3.78±0.39	242

a: Based on Gaia DR3 data
b: Offset from the center of Tapia's Globule #2, at RA,Dec=12:31:29.0, -63:44:48
c: Star not identified in [JHR80], but located close to [JHR80] D-19

curve parameters of interstellar polarization. The observations were planned such that, wherever possible, secondary stars were observed in addition to the main target, by rotating the spectroscopic slit.

The *polSALT* data reduction package (K. Nordsieck & D. Groenewald, 2024, private communications) has been developed by the SALT polarimetry team to perform the best possible systematic data reduction. We employed this software for the data reduction in this work. During the data reduction, careful attention was given to ensure that the source extraction-, and background-, windows were not contaminated by any secondary star in the vicinity of the target or contribution by the second order spectrum from the grating.

The output of *polSALT* consists of a table of values of p(λ), $\theta(\lambda)$, q(λ), and u(λ), for a user-selected set of wavelength bins, along with the error bars based on photon noise estimates. The projected accuracy is 0.05 % per spectral resolution bin[2]. These output files were used with a **custom** analysis code (Sec. 3.3.2) to derive the polarization parameters.

For three of our stars ([JHR80] D-1, D-14 and D-20), the polarization changes rapidly (and rotates in position angle) towards the blue, reminiscent of Rayleigh scattering. (Note that, as is the case for [JHR80] D-1, the combination of two close-to perpendicular polarization components, can lead to a decrease in the observed polarization level.) Given that all observations were acquired after astronomical twilight in dark time, the presence of Rayleigh scattered light is surprising. However, especially for [JHR80] D-1 and D-20, between $\lambda\lambda$ 0.5-0.6 μm, the deviations from a single Serkowski function shape are high enough signal-to-noise that they are unlikely to be due to marginal quality data. As will be discussed in Appendix A, satellite infrared imaging (available at https://meteologix.com/za/satellite/south-africa) show that [cirrus] clouds were present in the vicinity of Sutherland on some observing dates.

Taking advantage of the slit rotation, **we were able to add one extra target in our observations of [JHR80] D-19, which we have designated "19B". In addition,** two of our targets (D-17 and D-20) were observed twice, once as the main target and at another time as the secondary star for each other. This allowed us to verify the robustness and accuracy of data reduction obtained from the *polSALT* software. Because of the complex polarimetric behaviour of SALT/RSS, it is interesting to explicitly compare the results for the two targets and off-axis. Table 4 shows the resulting Serkowski parameters for

[2] https://astronomers.salt.ac.za/wp-content/uploads/sites/71/2022/06/3170AM0013_Polarimetry_Observers_Guide_V1.2.pdf

the SALT/RSS observations (only, without H-band data) of the two stars. In this table, "A" corresponds to the observation where the star was on the optical axis and "B" corresponds to the complementary observation where the other star was on the axis. The row without A or B shows the weighted average of the two measurements. The pairs of p_{max} and λ_{max} values are within each other's 1σ uncertainties. The only measurement pair not in very good agreement is the position angles for [JHC80] D-17. We note, however, that the "Rayleigh" term in the extracted [JHC80] D-17B and [JHC80] D-20A spectra are significant (0.59±0.07 and 0.38±0.03 %), and show consistent position angles (86±4° and 84±2°).

3 ANALYSIS

3.1 Extinction vs. Grain Heating

To probe the influence of geometry and other sources of "anomalous extinction" (i.e. where the observed A_V might not accurately reflect the radiation field damping seen by the grains responsible for the polarization), we follow AP07 and plot the I(60μm)/I(100μm) ratio vs. A_V for our sample. Figure 1 shows that the expanded sample of lines of sight **(combining the AP07 data and the present observations)** have a similar distribution as the AP07 data, with most of the lines of sight located around the "nominal" relationship defined in AP07, but with both high and low outliers. **We stress that, as noted in AP07, the exact locations of the two lines are somewhat uncertain.** For large A_V values ($A_V \gtrsim 3.5$ mag.) the FIR(A_V) ratio flattens out, as would be expected deep inside a starless cloud. We note that the wavelengths that efficiently heat the grains and those that can align them, are not necessarily the same. Specifically, if we assume that the largest grains in the cloud have a_{max}=0.45 μm, then the extinction for the light capable of aligning those largest grains is $A_{0.9\mu m}$=2.2 mag. (assuming R_V=5; Cox 2000, p.528), or only ~9% of the unattenuated flux, **thus potentially leaving a non-negligible grain-aligning flux at this extinction level**.

3.2 1.9m/HIPPO

We fitted Serkowski (and Wilking) functions to our UBVRI HIPPO polarimetry, using error-weighted fits in the Kaleidagraph software [3]. Using an F-test procedure (e.g. Lupton 1993), we evaluated the

[3] www.synergy.com

Table 3. 1.9m HIPPO Results

Star	p_U	θ_U	p_B	θ_B	p_V	θ_V	p_R	θ_R	p_I	θ_I
CPD-64 1900	0.41±0.10	115±1	0.43±0.09	91±6	0.44±0.09	84±7	0.17±0.09	89±16	0.24±0.10	108±3
HD 108417	0.35±0.10	76±11	0.77±0.09	81±4	0.63±0.09	74±6	0.67±0.09	80±5	0.78±0.09	76±4
HD 108418	1.28±0.10	79±3	1.82±0.09	80±2	1.83±0.09	75±2	1.77±0.09	77±2	1.62±0.09	80±2
HD 108804	0.46±0.10	64±9	0.82±0.09	73±5	1.08±0.09	67±2	0.77±0.07	72±3	0.88±0.08	72±3
HD 108813	0.14±0.10	149±26	0.04±0.08	124±34	0.09±0.09	110±3	0.13±0.07	158±23	0.30±0.08	87±8
HD 109065	0.57±0.09	79±6	0.94±0.08	80±3	1.06±0.09	70±3	1.04±0.09	70±3	1.02±0.10	76±4
CPD-64 1975	2.74±0.14	84±2	4.01±0.10	82±1	4.56±0.10	83±1	4.27±0.09	83±1	4.08±0.10	85±1
HD 109891	1.10±0.10	76±3	1.50±0.09	73±2	1.72±0.09	72±2	1.44±0.08	75±2	1.59±0.09	77±2
HD 109937	2.27±0.10	83±1	2.93±0.09	81±1	3.31±0.09	78±1	3.54±0.08	80±1	3.44±0.07	79±1
CPD-64 1976	2.23±0.21	72±4	3.63±0.10	72±1	3.98±0.10	72±1	3.89±0.10	73±1	3.94±0.09	76±1
HD 110102	1.77±0.16	64±4	2.46±0.09	64±2	2.79±0.10	66±1	2.54±0.09	67±1	2.40±0.10	70±2
HD 110151	1.17±0.10	80±3	1.58±0.09	80±2	1.72±0.08	74±1	1.66±0.09	78±2	1.80±0.09	78±2
HD 110245	1.04±0.11	119±1	1.06±0.09	121±1	1.12±0.07	117±2	1.29±0.07	121±2	1.21±0.07	121±2
HD 110432	1.42±0.07	90±1	1.62±0.09	95±1	1.84±0.07	86±1	1.70±0.08	80±2	1.80±0.07	84±1
HD 110433	1.90±0.15	81±2	2.52±0.09	77±1	2.73±0.09	73±1	2.90±0.08	76±1	2.76±0.11	76±1
HD 110498	2.05±0.10	90±1	2.43±0.09	89±1	2.65±0.10	86±1	2.38±0.09	85±1	2.42±0.09	87±1
HD 110660	2.09±0.10	79±2	2.80±0.08	78±1	2.96±0.08	77±1	2.80±0.09	77±1	2.83±0.10	76±1
HD 110715	2.14±0.11	78±2	2.54±0.09	76±1	2.75±0.09	74±1	2.67±0.09	74±1	2.76±0.10	77±1
HD 110737	0.94±0.10	71±4	1.36±0.08	69±2	1.73±0.09	68±2	1.72±0.07	70±2	1.87±0.07	69±2
HD 110946	1.78±0.12	77±3	2.29±0.09	77±2	2.30±0.09	77±2	2.43±0.09	78±1	2.30±0.11	77±2
HD 110984	4.17±0.15	92±0.9	5.01±0.07	90±0.4	5.65±0.08	89±0.4	5.51±0.07	89±0.4	5.14±0.08	93±0.4
HD 111024	0.39±0.11	3±7	0.48±0.08	40±4	0.60±0.08	47±4	0.34±0.08	125±7	0.55±0.09	55±5
CPD-64 2006	0.56±0.09	100±3	0.78±0.07	95±2	0.79±0.08	95±2	0.90±0.08	98±2	0.71±0.10	104±2
HD 111174	0.51±0.10	39±4	0.94±0.11	52±4	0.99±0.09	47±3	0.89±0.08	47±3	0.87±0.08	53±3
HD 111237	1.51±0.13	67±4	1.76±0.09	68±2	1.97±0.09	68±2	1.77±0.09	65±2	1.73±0.07	73±2
HD 111303	0.44±0.10	77±8	0.91±0.09	70±4	0.88±0.08	75±4	0.71±0.09	76±5	0.88±0.07	75±3
HD 111343	3.44±0.20	77±2	3.83±0.09	79±1	4.31±0.09	76±1	4.17±0.13	78±1	4.06±0.14	79±1
HD 111688	1.53±0.11	51±2	1.90±0.08	52±2	2.43±0.09	51±1	2.31±0.09	50±1	2.38±0.10	49±1
HD 111779	1.44±0.10	68±3	1.88±0.09	62±2	2.19±0.09	58±2	1.71±0.08	62±2	1.86±0.10	62±2
HD 111827	1.28±0.09	93±2	1.67±0.09	84±2	1.80±0.07	83±1	1.90±0.09	87±2	1.77±0.08	87±1
HD 111992	1.53±0.11	51±2	2.07±0.08	56±1	2.24±0.09	52±1	2.08±0.07	55±1	1.96±0.08	59±2
HD 112225	0.68±0.07	97±3	0.80±0.05	92±2	0.73±0.06	87±2	0.78±0.06	92±2	0.76±0.05	92±2
HD 112295	3.49±0.09	66±1	4.55±0.09	65±1	5.16±0.07	65±1	5.22±0.08	64±1	5.00±0.08	67±1
HD 112637	0.82±0.10	58±5	1.32±0.09	57±3	1.29±0.08	54±2	1.16±0.06	52±2	1.14±0.10	59±3
HD 112661	1.65±0.11	72±3	1.98±0.09	73±2	2.02±0.09	72±2	1.93±0.08	71±2	1.93±0.08	71±2
HD 112785	0.95±0.07	131±2	0.85±0.06	126±2	0.70±0.06	135±3	0.91±0.06	139±2	0.82±0.06	135±2
HD 112954	1.83±0.10	42±1	2.12±0.08	44±1	2.39±0.09	43±1	2.45±0.07	43±1	2.19±0.07	42±1
HD 113014	0.75±0.11	92±4	1.13±0.08	83±2	1.13±0.07	80±2	0.95±0.08	85±2	1.01±0.09	85±3
HD 113034	3.95±0.14	81±1	4.49±0.10	80±1	5.04±0.09	80±1	5.11±0.09	84±1	4.78±0.08	84±1
HD 113348	1.07±0.13	87±4	1.54±0.09	86±2	1.67±0.08	85±1	1.64±0.08	87±2	1.70±0.09	89±2
HD 113511	3.12±0.12	91±1.0	3.72±0.09	88±0.7	3.87±0.06	89±0.5	3.89±0.10	87±0.8	3.75±0.10	91±0.7
HD 113541	0.70±0.10	97±3	0.74±0.10	85±4	0.89±0.10	77±4	0.80±0.07	82±3	0.77±0.09	82±4
HD 113742	1.88±0.10	85±2	2.46±0.09	83±1	2.46±0.09	80±1	2.38±0.06	81±1	2.46±0.09	83±1
CPD-61 3462	1.79±0.10	89±2	1.90±0.09	84±2	2.04±0.06	85±1	1.96±0.07	85±1	1.83±0.07	85±1
HD 113968	0.77±0.09	84±4	0.97±0.06	84±2	1.09±0.09	83±2	0.98±0.09	85±3	1.11±0.08	85±2
HD 114157	1.20±0.23	106±2	0.64±0.09	81±5	0.66±0.09	77±5	0.62±0.10	87±5	0.69±0.09	77±5
HD 114653	0.62±0.09	89±4	0.78±0.09	80±4	0.86±0.07	80±3	0.80±0.10	84±4	0.84±0.10	80±4
CPD-60 4528	1.28±0.08	51±2	1.66±0.08	53±2	1.82±0.09	56±2	1.69±0.08	52±2	1.62±0.07	55±2
HD 114718	0.96±0.08	77±2	1.29±0.06	75±1	1.35±0.06	72±1	1.36±0.06	77±1	1.55±0.06	73±1
HD 114720	0.99±0.12	90±3	1.01±0.09	87±3	1.16±0.09	86±2	0.98±0.09	90±3	1.28±0.09	86±2
HD 114719	0.74±0.13	85±6	1.22±0.09	82±3	0.91±0.09	76±4	0.97±0.07	75±3	1.01±0.07	80±2

statistical significance of the K parameter. Only for CPD-61 3462 was the parameter warranted **at the 95% confidence level (while for HD 113511 it was warranted at the 90% level)**. To minimize systematic uncertainties in the p_{max} and λ_{max} parameters, we fixed K at 1.15 for all other lines of sight. The best fit parameters are shown in Table 5.

3.3 SALT/RSS

3.3.1 Stellar and Extinction Parameters

We used the full-resolution Stokes I spectra from our SALT/RSS observations to estimate the spectral classes of these stars. The wavelength range of 5000-7500Å (i.e. including Balmer-α at λ6563Å) was utilized to compare normalized spectra from our observations to normalized spectra of the standard stars in Jacoby et al. (1984). While this spectral segment is not the conventional, or optimal, wavelength

Table 4. SALT/RSS Serkowski Fit Parameters - [JHR80] D-17 & [JHR80] D-20

Star	p_{max} [%]	λ_{max} [μm]	$< P.A. >$ [° [E of N]
[JHR80] D-17A	5.00 ± 0.06	0.75 ± 0.02	63.8 ±0.3
[JHR80] D-17B	5.10 ± 0.07	0.74 ± 0.02	60.8 ±0.2
[JHR80] D-17	**5.04 ± 0.05**	**0.75 ± 0.01**	**61.7 ±0.2**
[JHR80] D-20A	3.96 ± 0.05	0.91 ± 0.05	67.1 ±0.3
[JHR80] D-20B	4.04 ± 0.19	1.00 ± 0.21	67.0 ±1.1
[JHR80] D-20	**3.97 ± 0.05**	**0.91 ± 0.05**	**67.1 ±0.3**

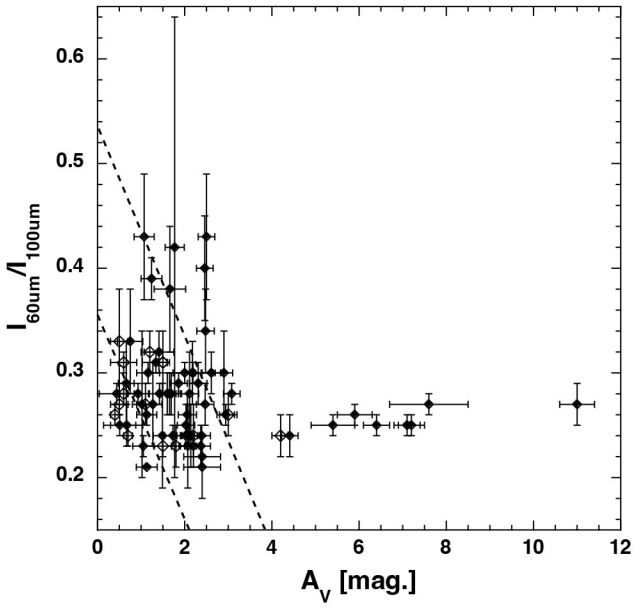

Figure 1. The ratio of I(60μm)/I(100μ) from the IRAS processing of IRAS data compared to the visual extinctions for each line of sight. Filled symbols correspond to the current sample, while open symbols correspond to the sample from AP07. The **region close to the nominal relationship, defined in AP07, including its dispersion** is shown by the two dashed lines. Also, the new sample is predominantly located in this nominal region, but with several outliers. As would be expected, for very large extinctions in this starless cloud, where the radiative heating of the dust is significantly diminished, the colour temperature reaches an asymptotic value.

range for spectral classification, we found that we could restrict the spectral classes to 1-2 subclasses for most stars. For two stars where there were more artifacts in the full-resolution data, we estimate uncertainties of up to 5 subclasses. These are noted with colons in Table 2, column 5. To better constrain the luminosity classes, we compared the trigonometric parallaxes from Gaia DR3 with the spectroscopic distances using our spectral classifications. For most of the target, we find that our nominal "giant" luminosity class (III) yields agreements within a factor 2-2.5 in distance. For two targets ([JHR80] D-4 and "D19-B") we assigned luminosity classes I and V, respectively, to avoid very large distance disagreements. For [JHR80] D-4 this luminosity classification (I) also has the advantage of moving the star out of the Hertzsprung gap for giants (lum. class III).

We extracted g- and r-band photometry from the "ATLAS" catalog (Tonry et al. 2018), which we transformed to B-V colours using the relations in Jester et al. (2005), as well as near-infrared (NIR) pho-

Table 5. Serkowski Fit Parameters - 1.9m/HIPPO targets

Star	p_{max} [%]	λ_{max} [μm]
CPD-64 1900	0.44 ± 0.09	0.35 ± 0.08
HD 108417	0.75 ± 0.06	0.7 ± 0.08
HD 108418	1.83 ± 0.05	0.57 ± 0.03
HD 108804	0.91 ± 0.05	0.65 ± 0.06
HD 108813[a]	<0.1	-
HD 109065	1.07 ± 0.06	0.68 ± 0.05
CPD-64 1975	4.41 ± 0.05	0.62 ± 0.01
HD 109891	1.62 ± 0.05	0.61 ± 0.03
HD 109937	3.54 ± 0.05	0.67 ± 0.01
CPD-64 1976	4.07 ± 0.05	0.64 ± 0.02
HD 110102	2.66 ± 0.05	0.59 ± 0.02
HD 110151	1.79 ± 0.05	0.65 ± 0.03
HD 110245	1.26 ± 0.04	0.62 ± 0.04
HD 110432	1.85 ± 0.04	0.6 ± 0.02
HD 110433	2.88 ± 0.05	0.64 ± 0.02
HD 110498	2.6 ± 0.05	0.57 ± 0.02
HD 110660	2.98 ± 0.05	0.6 ± 0.02
HD 110715	2.82 ± 0.05	0.61 ± 0.02
HD 110737	1.85 ± 0.06	0.75 ± 0.03
HD 110946	2.44 ± 0.05	0.6 ± 0.02
HD 110984	5.61 ± 0.04	0.6 ± 0.01
HD 111024	0.51 ± 0.04	0.58 ± 0.09
CPD-64 2006	0.84 ± 0.04	0.61 ± 0.06
HD 111174	0.93 ± 0.04	0.63 ± 0.05
HD 111237	1.91 ± 0.04	0.57 ± 0.02
HD 111303	0.88 ± 0.04	0.65 ± 0.05
HD 111343	4.32 ± 0.06	0.6 ± 0.02
HD 111688	0.42 ± 0.06	0.68 ± 0.02
HD 111779	1.98 ± 0.05	0.57 ± 0.02
HD 111827	1.87 ± 0.05	0.63 ± 0.03
HD 111992	2.17 ± 0.04	0.58 ± 0.02
HD 112225	0.82 ± 0.03	0.56 ± 0.03
HD 112295	5.26 ± 0.04	0.64 ± 0.01
HD 112637	1.23 ± 0.04	0.57 ± 0.04
HD 112661	2.07 ± 0.04	0.57 ± 0.02
HD 112785	0.91 ± 0.03	0.51 ± 0.03
HD 112954	2.42 ± 0.04	0.6 ± 0.02
HD 113014	1.1 ± 0.04	0.55 ± 0.04
HD 113034	5.14 ± 0.04	0.61 ± 0.01
HD 113348	1.72 ± 0.05	0.64 ± 0.03
HD 113511	3.98 ± 0.04	0.59 ± 0.01
HD 113541	0.85 ± 0.04	0.57 ± 0.05
HD 113742	2.52 ± 0.04	0.59 ± 0.02
CPD -61 3462[b]	2.06 ± 0.04	0.55 ± 0.02
HD 113968	1.1 ± 0.05	0.63 ± 0.04
HD 114157	0.71 ± 0.05	0.52 ± 0.07
HD 114653	0.87 ± 0.05	0.61 ± 0.06
CPD -60 4528	1.77 ± 0.04	0.59 ± 0.02
HD 114718	1.48 ± 0.04	0.67 ± 0.03
HD 114720	1.19 ± 0.05	0.63 ± 0.04
HD 114719	1.06 ± 0.04	0.56 ± 0.04

a: HD 108813 is, effectively, unpolarized.
b: Of the stars observed with HIPPO, only CPD-61 3462 formally (based on an F-test**at a 95% confidence level**) warrants using a "Wilking" fit - with the K-parameter as a free fitting parameter. For this star, with K free we find: p_{max}=2.02±0.05, λ_{max}=0.55±0.03, and K=0.73±0.28

tometry from the 2MASS survey (Cutri et al. 2003). Using intrinsic colours from the compilations in Cox (2000), we calculated colour excesses (E_{B-V}, E_{V-K}, E_{J-K}) and total-to selective extinctions, R_V (equ. 3). We calculated visual extinctions both from $E_{B-V} \cdot R_V$ and $E_{J-K} \cdot (5.82 \pm 0.$ Cox 2000, p.158). The visual extinctions based on the visual and NIR photometry are in good agreement, and we use the latter for this analysis (Table 2). For the three line of sights where Gaia DR3 A_0 values **(the monochromatic extinction at 0.548 μm (Creevey et al. 2023))** are available, we also list these in Table 2. They show reasonable agreement with our derived values. We note that the effective temperatures from Gaia DR3 are not always in agreement with our estimated spectral classes. However, the much hotter stellar types (~A8) implied by the quoted T_{eff} values for [JHR80] D-1 and D-19 are not compatible with the observed spectra.

For completeness, we used the g, r, i photometry from ATLAS (and transformations from Jester et al. (2005)), JHK photometry from 2MASS, and WISE photometry (Cutri & et al. 2012), together with the spectral classifications and intrinsic colors from Cox (2000) and Jian et al. (2017) to derive total-to-selective extinctions also from the relative extinction curves and the formula:

$$\frac{E_{\lambda-V}}{E_{B-V}} = \epsilon\lambda^{-\beta} - R_V \quad (4)$$

(e.g. Whittet 2003, p.81), see Figure 2. The two longest wavelength WISE bands (12.1 & 22.2 μm) may, as noted by Whittet (2003), primarily probe grain material characteristics, and may, therefore, affect the β parameter. But, as also noted by Whittet (2003), the best-fit R_V values are not strongly dependent on small variation in this parameter, and we have therefore retained all the bands in our fitting. Table 7 gives the best fit parameters. Column 5 of the table shows the R_V derived using the Whittet & van Breda (1978) approximation (Equ. 3). **For all targets, except 19B, the values derived by the two methods agree within their 1σ mutual uncertainty, while for 19B they agree within 2σ. This target has a late, and more uncertain, spectral class (K5 V:) and the lowest extinction of the SALT/RSS sample, $A_V \approx 2.8$.**

We note that the off-diagonal values of the covariance matrix for these fits are not zero, indicating some correlation between the variables. As our purpose with these fits is simply to validate the applicability of Equ. 3 for our sample, we will not pursue this issue, or the functional formulation by Martin & Whittet (1990), here.

3.3.2 *Polarization Parameters*

Because of what appears as an incomplete sky-polarization removal in the *polSALT* pipeline reduction, we developed an analysis code (in Python) to separate the ISM polarization ("Serkowski function") from possible "Rayleigh" scattering, nominally due to atmospheric effects (e.g.

Three data arrays for each star: wavelength [μm], q [%], and u[%], were used to generate the best fit combined Serkowski+Rayleigh function, yielding values for λ_{max}, p_{max}, K, θ_S, θ_R, and c (equ. 1 and 2). **We stress that the fitting was performed in q(λ), u(λ)) space, even though the results (e.g. Figure 3) are given in p(λ), $\theta(\lambda)$, through the standard transformations**

$$p = \sqrt{q^2 + u^2} \quad (5)$$

$$\theta = 1/2 \cdot \arctan(u/q) \quad (6)$$

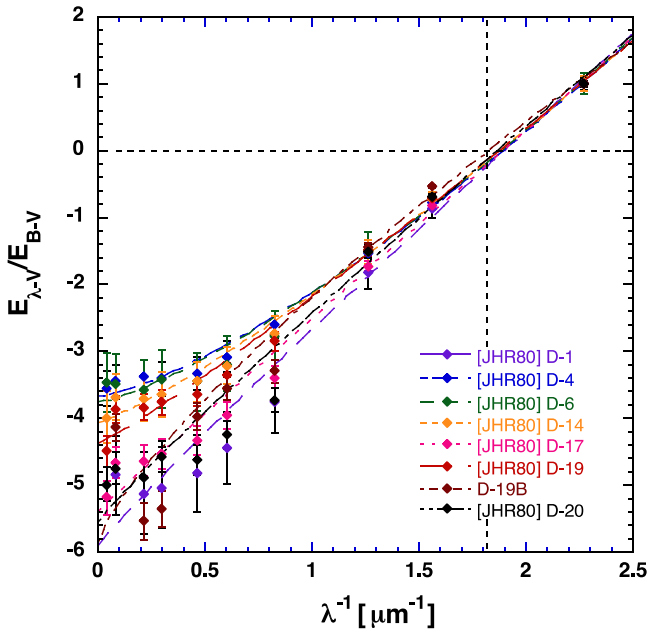

Figure 2. The normalized optical and infrared extinction curves for the SALT/RSS targets fitted by a standard functional form (equ. 3; Whittet (2003); Martin & Whittet (1990)). The points correspond to bands (right to left): B, R, I, J, H, K, W1, W2, W3, and W4. Because the uncertainty for E_{V-V}/E_{B-V} is undefined, we have not plotted these points. However, the dashed lines show where the point for V-band is located. The best-fit parameters are shown in Table 7.

For the combined fits shown in Figure 3, the best fit (q,u) parameters were added before transforming into (p, θ). Multiple synthetic data sets were created and used to test the code, confirming its effectiveness.

Where available, we included the H-band polarization from JHB84 in our polarization analysis of the SALT/RSS targets. Using an F-test (Lupton 1993) procedure for the SALT/RSS targets, we found that the inclusion of the K-parameter was not statistically warranted (at the 68% confidence level). To optimize the remaining parameters, we therefore set K=1.15 for all SALT/RSS targets.

Figure 3 shows the reduced polarization spectra with the best fit Serkowski function. Where the "Rayleigh" component was warranted/needed **(the c-parameter has an S/N > 3)** we have overlaid the best simultaneous fits of the two functions. Best fit **polarization** parameters are shown in Table 6.

4 RESULTS

Figure 4 shows the distribution of λ_{max} vs. A_V for the Southern Coalsack, overlaid on the results for the Taurus cloud from V20 (shown in orange), for comparison. Filled symbols represent the current data, while open symbols represent the results from AP07. Blue and red symbols, respectively, indicate lines of sight above **(and to the right of),** and below **and to the left** of the nominal I(60μm)/I(100μm) vs. A_V relationship **including the inherent dispersion** in Figure 1.

Several aspects of this plot are noteworthy:

- In contrast to the Taurus results, most of the Coalsack data reach an asymptotic value in λ_{max}, at small extinctions, of ~0.6μm
- The bifurcation in $\lambda_{max}(A_V)$ seen in Taurus is present also

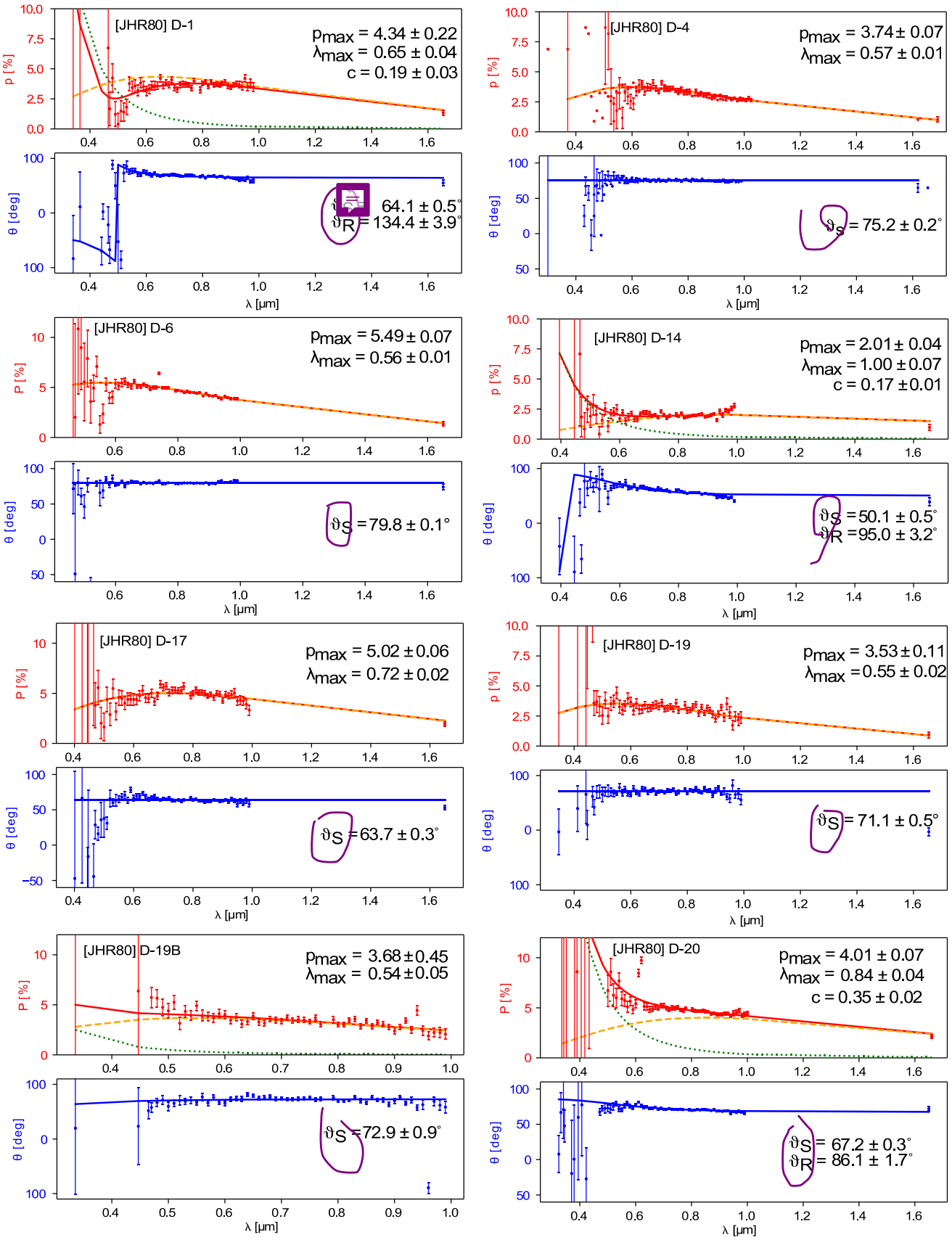

Figure 3. Polarization spectra of the stars observed with SALT/RSS are shown **together with H-band polarimetry from JHR84**, with best fit Serkowski (and, where required, nominally atmospheric Rayleigh) functions. For each star, the upper panel shows the polarization amount, with the Serkowski function shown in orange, the "Rayleigh" component in green and the combined fit in red. The lower panel shows the position angles with the Serkowski function in orange, the "Rayleigh" component in green and the combined fit in blue. We note that stars D-17 and D-20 were observed twice (as secondary stars in the other star's setting). Only one spectrum per star is shown here. The values listed in Table 6 are weighted averages of the two observations, and therefore differ from the values quoted (for one observation) in this figure. The derived parameters agree, **except for the PA values for [JHC80 D-17]**, within their 1-σ mutual

Table 6. Serkowski Fit Parameters - SALT/RSS target

	Serkowski Fit			Rayleigh Fit	
Star	p_{max} [%]	λ_{max} [μm]	$< P.A. >$ [° [E of N]	p_R [%]	P.A.$_R$ [° [E of N]
[JHR80 D-1]	4.34 ± 0.22	0.65 ± 0.04	64.1±0.5	0.19±0.03	134±4
[JHR80] D-4	3.74 ± 0.07	0.57 ± 0.01	75.2±0.2	-	-
[JHR80] D-6	5.49 ± 0.07	0.56 ± 0.01	79.8 ±0.1	-	-
[JHR80] D-14	2.01 ± 0.04	1.00 ± 0.07	50.1±0.5	0.17±0.01	95±3
[JHR80] D-17	5.07 ± 0.05	0.72 ± 0.01	61.8 ±0.2	-	-
[JHR80] D-19	3.53 ± 0.11	0.55 ± 0.02	71.1±0.5	-	-
D-19B[a]	3.68 ± 0.45	0.54 ± 0.05	72.9± 0.9	-	-
[JHR80] D-20	4.02 ± 0.07	0.82 ± 0.03	67.1 ± 0.3	0.35±0.02	86±2

a: SALT/RSS star for which H-band polarimetry is **not** available. This star was also not identified in [JHR80]

Table 7. Extinction Parameters - SALT/RSS target

Star	ϵ	β	R_V (fit)	R_V (WvB)[a]
[JHR80] D-1	3.2±0.6	0.9±0.1	5.9±0.6	5.3±0.5
[JHR80] D-4	1.6±0.2	1.4±0.1	3.7±0.1	3.7±0.4
[JHR80] D-6	1.6±0.3	1.3±0.2	3.8±0.3	3.8±0.5
[JHR80] D-14	1.9±0.2	1.2±0.1	4.1±0.2	3.8±0.4
[JHR80] D-17	2.9±0.1	1.0±0.1	5.4±0.1	4.8±0.3
[JHR80] D-19	2.2±0.3	1.1±0.1	4.4±0.3	4.0±0.4
D-19B	3.7±0.9	0.8±0.2	5.9±0.7	4.4±0.8
[JHR80] D-20	3.1±0.8	0.9±0.2	5.6±0.7	5.1±0.8

a: Using equation 3 (Whittet & van Breda 1978)

for the Southern Coalsack. The bifurcation point in the two sets are consistent with each other, although there are too few data points in the current Coalsack sample to evaluate this in detail. Two lines of sight are confidently located on the upper branch in the Coalsack: [JHR80] D-20 with A_V, λ_{max}={5.4±0.5, 0.82±0.03} and [JHR80] D-14 with A_V, λ_{max}={7.2±0.3, 1.00±0.07}

- As for Taurus, a broadening of the λ_{max} distribution is evident around A_V~2 mag. for the Coalsack. (Figure. 4)
- Finally, three of the "low" λ_{max} points at high extinction fall well below the extrapolation of the low-A_V $\lambda_{max}(A_V)$ relationship.

In addition, we find (Figure 5) total-to-selective extinctions, R_V, significantly greater than the diffuse ISM value of 3.1. Using weighted averages we find that for A_V=1-2 mag. $< R_V >$=4.3±0.1; for A_V=2-3 mag. $< R_V >$=3.9±0.7; for A_V=3-5 mag. $< R_V >$=4.13±0.1 and for A_V >5 mag. $< R_V >$=4.2±0.2. For the full A_V range we find $< R_V >$=4.01±0.05.

We expand on each of these results next.

4.1 Asymptotic $\lambda_{max}(A_V)$ at Small Extinctions

As discussed above, the lower size limit for aligned dust grains, under RAT alignment, is governed by either the reddening into the cloud and the alignment condition that the smallest aligned grain is given by the shortest remaining wavelength of the radiation field; $a_{min}^{align}=\lambda/2$, or by the collisional disalignment which depends linearly on the grain radius (such that the smallest grains disalign fastest).

We used the nominal $\lambda_{max}(A_V)$ relationship derived for the Coalsack by AP07

$$\lambda_{max} = (0.50 \pm 0.02) + (0.05 \pm 0.01) \cdot A_V \quad (7)$$

to compare and clarify the results from the I(60μm)/I(100μm) vs. A_V analysis of stars below A_V < 4.2 mag. If we select only those lines of sight that differ in $\mid \lambda_{max}(A_V) \mid$ from equation 4.1 by more than 2σ, we find that of the 12 lines of sight which fall below the nominal $\lambda_{max}(A_V)$ relationship, 7 show high negative FIR colour temperatures, 5 fall in the nominal I(60μm)/I(100μm) vs. A_V region, and none show a low FIR ratio. For the 15 lines of sight significantly above equation 4.1, 5 show low FIR ratios, 9 fall in the nominal I(60μm)/I(100μm) vs. A_V region, and 1 show a high FIR ratio.

Because a high (low) FIR(A_V) ratio indicates a line of sight where the effective opacity is lower (higher) than the measured **line-of-sight** extinction, these results - especially for the first group (low $\lambda_{max}(A_V)$ and high FIR ratios) - are consistent with a geometric origin of the outliers, such as where the line of sight probes inter-clump material, partially protected from the diffuse radiation field by surrounding clouds/clumps (type C in Figure 7 in AP07). The relatively large number of lines of sight with high $\lambda_{max}(A_V)$ but nominal FIR ratios, on the other hand, may indicate an additional mechanism increasing λ_{max} above the value expected from reddening into the cloud. As discussed in V20, localized increases in the gas space density and/or temperature, which preferentially disalign the smallest grains, can cause this effect. Given the mostly nominal values of the FIR ratios, density enhancements are more likely than significant temperature changes. As shown by V20 (their Figure 5c), a constant $\lambda_{max} \approx 0.6\mu$m at small A_V implies a gas density of $\sim 2 \cdot 10^4$ cm^{-3}

4.2 Bifurcation of $\lambda_{max}(A_V)$ at A_V >4

As in the Taurus cloud, the bifurcation in $\lambda_{max}(A_V)$ occurs at $A_V \approx 4$ mag. Additional data are needed to constrain this relative result further. However, the bifurcation, as such, is real. As shown by the modeling in V20, differences in λ_{max}, at a given A_V, can be caused by differences in the gas density of the material, and/or grain growth. With both spectral classifications and multi-band (importantly also blue light) photometry available we could derive the total-to-selective extinction of our target stars. Figure 5 shows the results as a function of the visual extinction. While some systematic structure is seen (especially beyond A_V=5 mag.), there is no systematic difference in R_V between the lines of sight on the "upper-" and "lower branches", indicating that the large values of λ_{max} on the upper branch are likely not due to specific grain growth caused by ice mantle formation. However, as we discuss below, the large upper grain size limits implied by the high R_V values are required for these large values of λ_{max}.

Figure 6 shows the polarization efficiency (p_{max}/A_V) for our target stars. A general negative trend is seen with increasing extinction for

the low and medium extinction targets. For a constant (and wavelength independent) grain alignment, and a fully turbulent magnetic field, a power-law drop-off with an exponent of -1/2 is expected (Jones et al. 1992). For regions where only a surface layer contributes to the polarization ("polarization hole"), a power-law exponent of -1 (i.e. p does not increase with A_V) is expected. These slopes are shown for illustrative purposes in the figure, but note that they are **not** fits to the data.

Because the alignment efficiency on different lines of sight, in the low-to-medium extinction medium, is **not** constant, as illustrated by the varying FIR ratios, and because different grain sizes experience different (dis)alignment strengths, we would not expect a simple power-law to apply to all lines of sight.

At visual extinctions beyond $A_V \approx 4$ mag., where the grain heating by the external field is unimportant, we find a well defined and very steep fall off in p_{max}/A_V, with a power-law exponent of -2.4±0.1, if all the lines of sight are included. If we use only the points on the lower branch to calculate the fit (Figure 7, black symbols) a power-law exponent of -1.4±0.1 is found. **The line of sight towards [JHR80] D-14, on the top of the upper branch, is at a significantly lower polarization efficiency than expected from this fit.**

Despite the very steep fall of the polarization efficiency, this does likely not indicate a simple "polarization hole" (where all grain alignment has ceased) at or near $A_V \approx 4$ mag., since that would leave also λ_{max} fixed. Grain alignment is, clearly, significantly decreased - more so for the smaller grains - but residual alignment is present, which can be further suppressed by enhanced collisions. The large offset for [JHR80] D-14 from the best-fit curve shows this.

Following Jones et al. (1980), we calculate the on-the-sky distance of the stars from the center of Tapia's Globule #2 (Table 2, column 10). As shown in Figure 6 of Jones et al. (1980), the core of the globule is detected to about 200″ from the center, meaning that in our sample only [JHR80] D-14 unambiguously probes the core of the globule as measured by NIR color excess. Further data are needed to establish whether ice-mantle mediated grain growth is taking place in any locations in the core, but our data support that λ_{max} traces the spatial gas density in the medium.

While the bifurcation at ~4 mag provides a drastic dispersion in $\lambda_{max}(A_V)$, similar effects are also seen at more moderate extinctions. As medium extinction ($A_V \approx 2$ mag) lines of sight into the cloud are probed, the smallest aligned grain is more often determined by the colour of the radiation field, and the linear dependence of λ_{max} on A_V is reestablished (for dense, low-extinction material as we see in the Coalsack). For inhomogeneous clouds, a mix of the two can occur, as seen in both Taurus and here, where for some extinctions a broadening of the $\lambda_{max}(A_V)$ relation is seen. This is prominent in the Taurus data at $A_V \approx 2$ mag, and also seen in our current results.

4.3 Low λ_{max} Values at High Extinctions

While there are several mechanism identified that can cause λ_{max} to increase beyond that expected from RAT alignment in a dark, quiescent cloud, decreasing λ_{max} at high A_V (again, in a star-less cloud) is not easily explained. Since the FIR color is constant for our sample beyond A_V=4 mag, implying that no internal radiation sources are present, we must seek other explanations for the unexpectedly low values of λ_{max} seen at $A_V > 7$ mag. in Figure 4.

Since many of our targets are at large distances, their polarization spectra may contain effects from material background to the Coalsack. Seidensticker & Schmidt-Kaler (1989) has argued that the near-side of the Carina arm is located at about 1.3 kpc, so most of the targets observed with SALT/RSS, and all of the ones with low λ_{max}

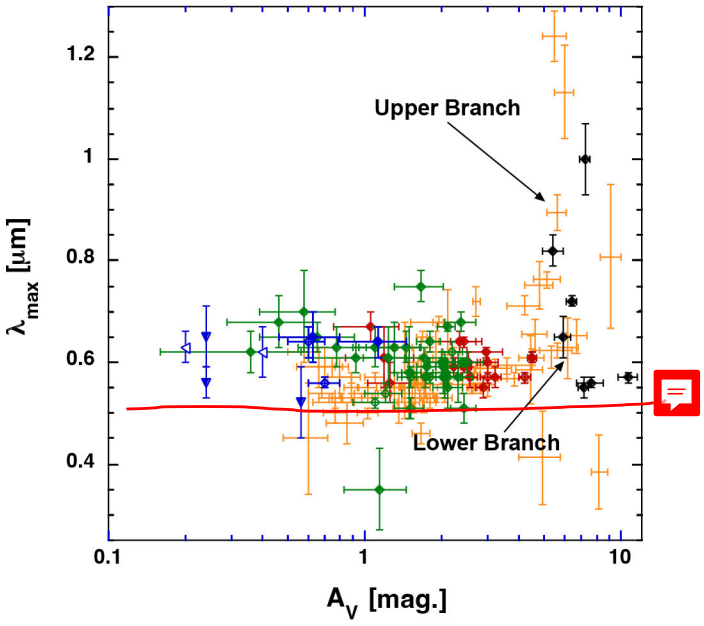

Figure 4. The locations of the polarization peak are shown as a function of visual extinction. Filled symbols correspond to our new observations with the 1.9m telescope and HIPPO. Open points correspond to observations with the same instrument from Andersson & Potter (2007). For the targets at A_V <3 mag, green symbols correspond to nominal values in the $I_{60}/I_{100}(A_V)$ relation, blue symbols to low values of I_{60}/I_{100} and red symbols to high values of I_{60}/I_{100}. Left-pointing triangles indicate 2σ upper limits on the visual extinction. Orange points correspond to the results for the Taurus molecular cloud from Vaillancourt et al. (2020) and are included for direct comparison between the clouds.

values at $A_V > 7$ mag., are located in or behind the Carina arm. The large scale magnetic field in the Galaxy follows the spiral arms (Heiles 1996; Brown 2010, and refs. therein), so we would, generally, expect such background polarization to be along the Galactic plane.

Because the position angles in Equatorial and Galactic coordinates (in the direction of the Coalsack) differ by less than 5°, polarization from the Carina arm (and the **average** Galactic field direction) should be detectable, if the polarization signal is strong enough. If the dust in the Carina arm has a significantly smaller a_{min}^{align}, and therefore smaller inherent λ_{max}, than the dust at large extinction in the Coalsack, the polarization signal from the background could enhance the observed polarization at shorter wavelength and should then rotate the position angles to smaller values, even allowing for polarimetric radiative transfer effects in the Coalsack envelope. (For longer wavelengths where the larger grains dominate, any signal from the background is likely to be unimportant)

We reviewed the residuals in position angles from our spectral fitting at the shorter wavelengths in our SALT/RSS data. Because of the systematic uncertainties introduced by the nominally atmospheric Rayleigh scattering (and decreasing instrumental sensitivities), we could only evaluate these effects down to ~5000Å. No clear systematic trends beyond ~5-10° are present, it therefore seems unlikely that the small λ_{max} values seen at A_V >7 mag. are due to background polarization. **As Table 3 shows, the position angles for the Hippo targets vary significantly, with the bulk of targets showing 45° <P.A.< 100 °. Polarization along the Galactic plan would be consistent with the higher part of this range. However, also many targets at d<1 kpc show such position angles.**

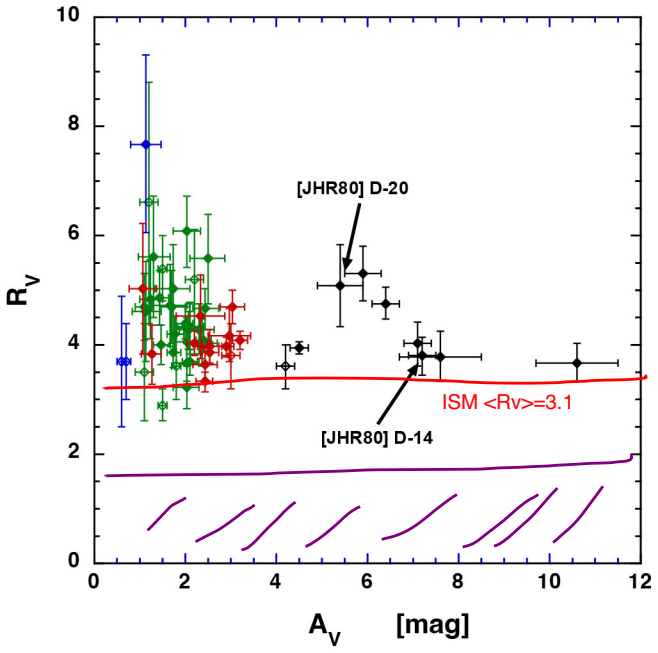

Figure 5. The derived values of the total-to-selective extinction versus visual extinction using the approximation R_V=1.1·E_{V-K}/E_{B-V} (Whittet & van Breda 1978). Symbols are as in Figure 4. The two stars in the "upper branch" in that figure are noted by arrows. Surprisingly, the R_V values on the "upper branch" in Figure 4 are not systematically different from those on the "lower branch".

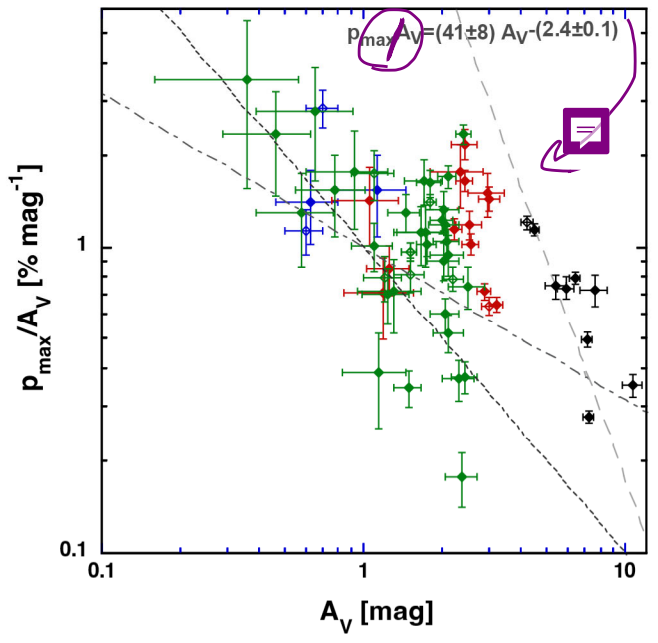

Figure 6. The polarization efficiency (p_{max}/A_V) is shown as a function of the visual extinction. The dashed and dash-dotted lines (**best fits**) indicate power-law exponents of -1 and -0.5, respectively (see text for discussion). The solid line shows a power-law fit to all stars with A_V >4 mag. (where the FIR ratio is constant).

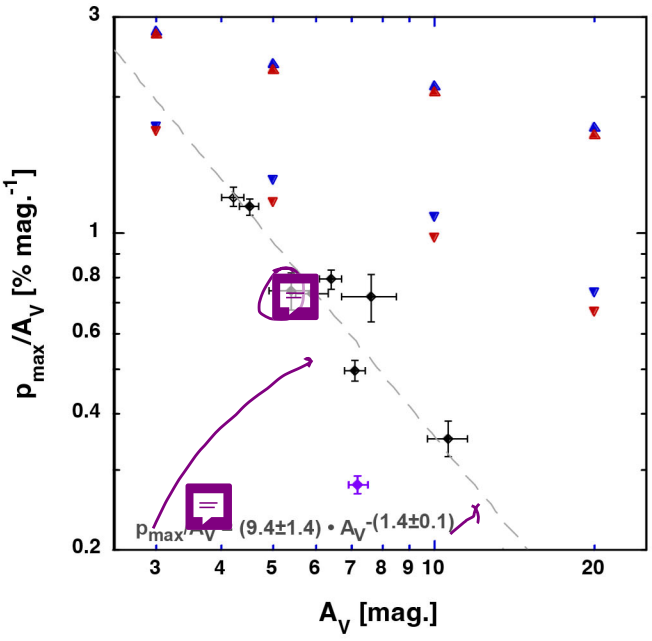

Figure 7. The polarization efficiency (p_{max}/A_V) is shown as a function of A_V for stars with A_V >4 mag. The dashed line represents a weighted fit for the lines of sight on the lower branch in Figure 4 (black symbols). The line of sight on the upper branch ([JHR80] D-14) is plotted with purple symbols. All lines of sight on the lower branch lie within 2.6σ (usually within 1σ) of the best fit line. The polarization efficiency for [JHR80] D-14 deviates by 20σ from the fit. Red and blue symbols represent the theoretical predictions for a star-less molecular cloud with and without radiative grain destruction (RAT-D), respectively (Lee et al. 2020) (see text for details).

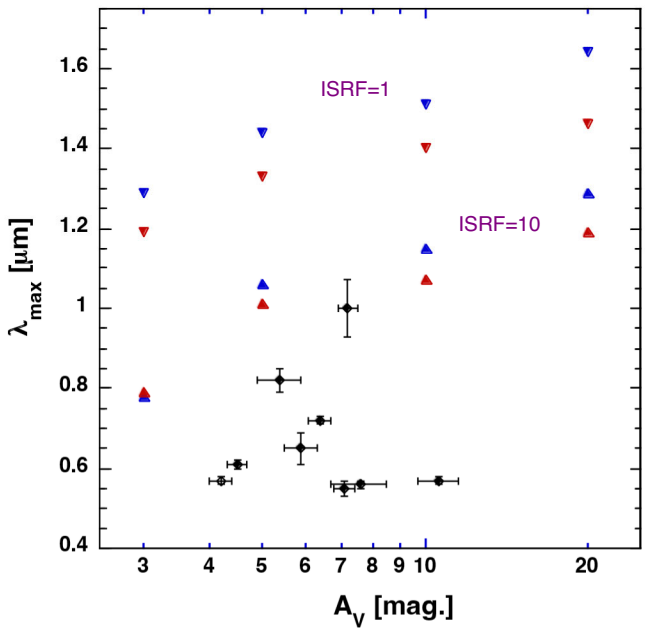

Figure 8. The location of the polarization peak (λ_{max}) is shown as a function of A_V for stars with A_V >4 mag. Red and blue symbols as in Figure 7.

5 DISCUSSION

Our comparison of the Coalsack and Taurus polarimetry data shows that the two data sets agree closely at A_V >1.5 mag., with a similar bifurcation in the $\lambda_{max}(A_V)$ relation at A_V ~4 mag., and a broadening of the $\lambda_{max}(A_V)$ distribution at around A_V ~2 mag. Two of our Coalsack lines of sight ([JHR80] D-14 and [JHR80] D-20) are located on "the upper branch" showing the existence of this effect also in the Coalsack. The locations on the sky of [JHR80] D-14, inside the outline of Tapia's Globule #2 (the central core of the Southern Coalsack) as mapped by JHB84, is consistent with the findings of Vaillancourt et al. (2020) that the "upper branch" corresponds to volumes of high space-density material, at high visual extinction. The on-the-sky offset for [JHR80] D-20, and it's more moderate visual extinction, are consistent with its somewhat lower λ_{max}, but still indicate an enhanced gas density on this line of sight.

While no enhancement is seen in the total-to-selective extinction (R_V) for the upper branch, the average value of R_V in the Southern Coalsack is significantly greater, $< R_V >$=4.0±0.1 (weighted average for A_V=1-5 mag.), than the typical value for the ISM of 3.1 (Whittet 2003). Based on the analysis of the ρ Oph line of sight (R_V=4.4) Mathis & Wallenhorst (1981) found an upper limit on the grain size distribution closer to a_{max}=0.4-0.5 μm. Thus, the generally large values derived for R_V indicate that the maximum grain sizes in the Coalsack are larger than the typical ISM value of a_{max}=0.3 μm, even at moderate extinctions.

We compared our observational polarization curves to the theoretical predictions for a star-less molecular cloud from Lee et al. (2020), (Figures 7 and 8). In these figures blue symbols indicate calculations without radiatively driven grain disruption (RAT-D; Hoang et al. 2019), while red symbols indicate calculations including the RAT-D effect. Downward pointing triangles correspond to the average energy density in the local interstellar radiation field (u_{ISRF}=1), while upward pointing triangles correspond to u_{ISRF}=10 (Lee et al. 2020).

We find that the the theoretical curves in Lee et al. (2020) show both too large λ_{max} and too large p_{max}/A_V compared to the data. While the stronger radiation field models come closer to matching the observed values of λ_{max}, they make the mismatch in polarization efficiency worse. The slope in p_{max}/A_V vs. A_V is also too shallow in the theoretical calculations - even for the "lower branch" lines of sight. As expected for a dense star-less cloud, the RAT-D effect makes very little difference, and does not help the calculations match the observations.

The likely explanation for this mismatch originates in the choice by Lee et al. (2020) to set the upper boundary on the grain size distribution at 1.0 μm (Hoang, 2024, private communications). Because the RAT alignment condition is a lower limit on the wavelength ($\lambda_{align} < 2\,a$) and because the extinction decreases towards longer wavelengths, larger grains will be aligned if smaller ones are - unless strong radiative disruption is present. Hence reconciling the theoretical models with our data requires a smaller value of a_{max} than assumed by Lee et al. (2020).

As noted above, our derived values of R_V ~3.5-5 for the deep lines of sight imply a_{max} of ~0.4-0.5 μm. A fairly sharp upper size cut off at this radius would yield smaller λ_{max} values and a steeper slope in p_{max}/A_V vs. A_V, than allowing the size distribution to continue to larger radii. It is noteworthy that for the two stars on the upper branch, [JHR80] D-14 has the smaller R_V value of 3.9±0.2, while [JHR80] D-20 has R_V=5.1.±0.6.

Such a smaller value of a_{max} (a_{max} ~0.4μm, rather than ~1.0μm) is also supported by comparing the polarization efficiency (Figure 7) to the calculations by Hoang et al. (2021), especially for [JHR80] D-14. Their Figure 5 shows that grains with a ~0.4-0.5 μm, at A_V=7 mag. are collisionally disaligned at a gas density of n_H=10^5-10^6 cm^{-3}. The steep slope in $p_{max}/A_V(A_V)$ (Figure 7), even on the lower branch (power-law exponent <-1), indicates that the reddening is moving a_{align} close to a_{max} and hence the loss in polarization efficiency is dominated not by the alignment efficiency of the still aligned grains, but rather the size fraction of remaining aligned grains.

A sharp cutoff at a_{max}=0.4-0.5 μm would also explain the significant deficit in p_{max}/A_V for [JHR80] D-14, on the upper branch, as the additional collisional disalignment on this line of sight would then come very close to disalign all the grains (up to a_{max}) and hence fully destroying the generation of polarization in the dense gas. For [JHR80] D-20 with a larger R_V and lower A_V, the collisional disalignment, even at the higher density of the upper branch, would not have been close enough to a_{max} to generate the steeper drop in p_{max}/A_V.

Whether additional, ice-mantle enhanced, grain growth is present in the Coalsack is not clear from our data. Smith et al. (2002) measured the water ice line at 3.08μm towards 6 background stars in the Coalsack. They only detected the line at more than 2σ for two stars: [JHR80] D-7 (110″from the globule center; compared to a distance for [JHR80] D-14 of 169″) and, marginally (at 2.33σ), for [JHR80] E-18 (well away from the globule core, but possibly probing a secondary density maximum). Further, and likely even deeper, spectro-polarimetric data are needed to address the relationship between ice mantles and grain growth in the Coalsack.

A space density of n_H=10^5-10^6 cm^{-3} for the upper branch indicates that the clump-interclump gas density contrast varies in the cloud. In the low-to-medium extinction region (A_V < 4 mag.) the density contrast is of the order 100, while in the high extinction range (A_V > 4 mag.) it is then closer to 10^4.

Also for low extinctions (A_V <1.5 mag) the Southern Coalsack and Taurus show similarities, except that the collisional effects are stronger in the former, indicating a gas density of several times 10^4 cm^{-3} on the moderate extinction sight lines in the Coalsack. Such an elevated gas density is consistent with the compression of the cloud by the Upper Centaurus-Lupus super bubble discussed before. Both because the collision rate only depends on the gas temperature as $\sqrt{T}$ and because relatively higher values of λ_{max} are not strongly associated with large ratios of I(60μm)/I(100μm) (Sec. 4.1), we conclude that the high (constant) value of λ_{max} is due to enhance gas density, rather than heating.

As noted in the results section, the low values of λ_{max} for the three most highly extincted stars on the lower branch is surprising. While no position angle rotation (indicating a background polarization component with θ_{Gal} ≈90°) is evident in our data, these do not effectively extend below ~5000Å. Higher quality, short wavelength data may resolve this issue.

6 SUMMARY AND CONCLUSIONS

We have used multiband- and spectro-polarimetry of stars behind the Southern Coalsack, from the SAAO 1.9m/HIPPO and SALT/RSS, to study the dependence of the polarization curves with extinction. Our sample contains 74 lines of sight spanning A_V=0.4-10.6 mag. We find that:

- A similar bifurcation in $\lambda_{max}(A_V)$ as seen in the Taurus clouds (V20) is present also in the Southern Coalsack, indicating a clumpy structure where collisional disalignment is responsible for the large values of λ_{max} on the "upper branch" of the bifurcation.

- The total-to-selective extinction in the cloud, both at moderate and high extinctions, is $R_V \approx$4-5.
- The R_V values on the upper and lower branches of $\lambda_{max}(A_V)$ (for A_V >4) are not systematically different, indicating that grain growth is not the dominant cause of the upper branch in the Coalsack. However, to allow high gas densities and intense collisional disalignment to produce the large λ_{max} values on the upper branch large grains (up to $a \approx 0.4 - 0.5\mu$m) must be present, as is indicated by the large derived R_V values.
- For the line of sight at the top of the upper branch we find a significant decrease in the polarization efficiency (p_{max}/A_V) relative to the other high extinction line of sight. This is consistent with the size of the smallest aligned grain starting close to the upper end of the [total] grain size distribution for this target, and indicating a fairly sharp cut-off in grain size at a_{max}=0.4-0.5 μm. This line of sight is, also, the one in our sample probing the core of Tapia's Globule #2, as delineated by Jones et al. (1980) The other target on the upper branch has both lower A_V and larger R_V such that even with higher gas densities, the collisional disalignment does not reach a_{max} for this line of sight.

- Because the Southern Coalsack is star-less, this upper limit on the grains sizes implies that the RAT-D effect is not ~~required to limit~~ important in limiting the large grain population.
- At low extinctions the Coalsack mostly shows constant $\lambda_{max}(A_V)$ values of ~0.6 μm, indicating a gas density of $\sim 2 \cdot 10^4$ cm^{-3} in the outer part of the cloud.
- Some of the lines of sight on the lower branch show λ_{max} values significantly below what would be expected from RAT alignment of a standard MRN grain size distribution. The cause of this is unclear, but does not seem to be due to background contamination.

ACKNOWLEDGEMENTS

We gratefully acknowledge the help of Prof. Ken Nordsieck and Dr. Danielè Groenwalt in understanding the RSS instrument, the *polSALT* pipeline and the processing of SALT/RSS polarimetry observations. We thank Profs. Thiem Hoang and Alex Lazarian for helpful discussions. The U.S. National Science Foundation provided financial support for B-G A and KRK through grant AST-1715876. AM gratefully acknowledges financial support from a Fox Fellowship from the Physics Department of SCU.

This publication makes use of data products from the Wide-field Infrared Survey Explorer, which is a joint project of the University of California, Los Angeles, and the Jet Propulsion Laboratory/California Institute of Technology, funded by the National Aeronautics and Space Administration.

DATA AVAILABILITY

The reduced HIPPO data are given in Table 3. Raw RSS data are available from the SAAO/SALT Data Archive (https://ssda.saao.ac.za/) and reduced data by request from the authors. The *polSALT* pipeline is described on the SAAO website and can be down-loaded from GitHub at (https://github.com/saltastro/polsalt). The fitting routine, used to derive polarization parameters for the RSS spectra is available by request from the authors.

REFERENCES

Andersson B.-G., Potter S. B., 2005, MNRAS, 356, 1088
Andersson B.-G., Potter S. B., 2007, ApJ, 665, 369
Andersson B.-G., Wannier P. G., 1997, ApJ, 491, L103
Andersson B.-G., Knauth D. C., Snowden S. L., Shelton R. L., Wannier P. G., 2004, ApJ, 606, 341
Andersson B.-G., et al., 2013, ApJ, 775, 84
Andersson B.-G., Lazarian A., Vaillancourt J. E., 2015, ARA&A, 53, 501
Bailer-Jones C. A. L., Rybizki J., Fouesneau M., Mantelet G., Andrae R., 2018, AJ, 156, 58
Boogert A. C. A., Gerakines P. A., Whittet D. C. B., 2015, ARA&A, 53, 541
Brown J. C., 2010, in Kothes R., Landecker T. L., Willis A. G., eds, Astronomical Society of the Pacific Conference Series Vol. 438, The Dynamic Interstellar Medium: A Celebration of the Canadian Galactic Plane Survey. p. 216 (arXiv:1012.2932), doi:10.48550/arXiv.1012.2932
Clayton G. C., Wolff M. J., Sofia U. J., Gordon K. D., Misselt K. A., 2003, ApJ, 588, 871
Cox A. N., 2000, Allen's astrophysical quantities. Allen's astrophysical quantities, 4th ed. Publisher: New York: AIP Press; Springer, 2000. Edited by Arthur N. Cox. ISBN: 0387987460, http://adsabs.harvard.edu/cgi-bin/nph-bib_query?bibcode=2000asqu.book.....C&db_key=AST
Crawford I. A., 1995, MNRAS, 277, 458
Creevey O. L., et al., 2023, A&A, 674, A26
Cropper M., 1985, MNRAS, 212, 709
Cutri R. M., et al. 2012, VizieR Online Data Catalog, p. II/311
Cutri R. M., et al., 2003, VizieR Online Data Catalog, 2246, 0
Draine B. T., Lazarian A., 1998, ApJ, 508, 157
Ducati J. R., Bevilacqua C. M., Rembold S. B., Ribeiro D., 2001, ApJ, 558, 309
Duncan A. R., Haynes R. F., Jones K. L., Stewart R. T., 1997, MNRAS, 291, 279
Fitzgerald M. P., 1970, A&A, 4, 234
Heiles C., 1996, in Roberge W. G., Whittet D. C. B., eds, Astronomical Society of the Pacific Conference Series Vol. 97, Polarimetry of the Interstellar Medium. p. 457
Hennebelle P., Whitworth A. P., Goodwin S. P., 2006, A&A, 451, 141
Hoang T., Tram L. N., Lee H., Ahn S.-H., 2019, Nature Astronomy, 3, 766
Hoang T., Tram L. N., Lee H., Diep P. N., Ngoc N. B., 2021, ApJ, 908, 218
Høg E., et al., 2000, A&A, 355, L27
Houk N., Cowley A. P., 1975, Michigan Catalogue of two-dimensional spectral types for the HD star. Ann Arbor: University of Michigan, Department of Astronomy, 1975, http://adsabs.harvard.edu/cgi-bin/nph-bib_query?bibcode=1975mctd.book.....H&db_key=AST
Jacoby G. H., Hunter D. A., Christian C. A., 1984, ApJS, 56, 257
Jester S., et al., 2005, AJ, 130, 873
Jian M., Gao S., Zhao H., Jiang B., 2017, AJ, 153, 5
Jones T. J., 1989, ApJ, 346, 728
Jones T. J., Hyland A. R., Robinson G., Smith R., Thomas J., 1980, ApJ, 242, 132
Jones T. J., Hyland A. R., Bailey J., 1984, ApJ, 282, 675
Jones T. J., Klebe D., Dickey J. M., 1992, ApJ, 389, 602
Kastner J. H., Weintraub D. A., 1994, ApJ, 434, 719
Kim S.-H., Martin P. G., 1995, ApJ, 444, 293
Lada C. J., Huard T. L., Crews L. J., Alves J. F., 2004, ApJ, 610, 303
Lazarian A., Hoang T., 2007, MNRAS, 378, 910
Lebreuilly U., Commerçon B., Laibe G., 2020, A&A, 641, A112
Lee H., Hoang T., Le N., Cho J., 2020, ApJ, 896, 44
Lupton R., 1993, Statistics in theory and practice. Princeton, N.J.: Princeton University Press, http://adsabs.harvard.edu/cgi-bin/nph-bib_query?bibcode=1993stp..book.....L&db_key=AST
Marchand P., Tomida K., Tanaka K. E. I., Commerçon B., Chabrier G., 2020, ApJ, 900, 180
Martin P. G., Whittet D. C. B., 1990, ApJ, 357, 113
Mathis J. S., Wallenhorst S. G., 1981, ApJ, 244, 483
Mathis J. S., Rumpl W., Nordsieck K. H., 1977, ApJ, 217, 425
Nyman L., 2008, The Southern Coalsack. pp 222–+

Nyman L.-A., Bronfman L., Thaddeus P., 1989, A&A, 216, 185
O'Donoghue D., et al., 2006, MNRAS, 372, 151
Olofsson G., Nilsson R., Florén H. G., Djupvik A., Aberasturi M., 2012, A&A, 544, A43
Ormel C. W., Paszun D., Dominik C., Tielens A. G. G. M., 2009, A&A, 502, 845
Ossenkopf V., 1993, A&A, 280, 617
Paladini R., et al., 2021, Unveiling Grain Growth in Very Dense Galactic Cores, JWST Proposal. Cycle 1, ID. #2331
Potter S., et al., 2008, in Society of Photo-Optical Instrumentation Engineers (SPIE) Conference Series. , doi:10.1117/12.789716
Potter S. B., et al., 2016, in Evans C. J., Simard L., Takami H., eds, Society of Photo-Optical Instrumentation Engineers (SPIE) Conference Series Vol. 9908, Ground-based and Airborne Instrumentation for Astronomy VI. p. 99082K, doi:10.1117/12.2232391
Seidensticker K. J., 1989, A&AS, 79, 61
Seidensticker K. J., Schmidt-Kaler T., 1989, A&A, 225, 192
Serkowski K., 1973, in IAU Symp. 52: Interstellar Dust and Related Topics. p. 145, http://adsabs.harvard.edu/cgi-bin/nph-bib_query?bibcode=1973IAUS...52..145S&db_key=AST
Shenoy S. S., 2003, PhD thesis, Rensselaer Polytechnic Institute
Skiff B. A., 2014, VizieR Online Data Catalog, p. B/mk
Smith R. G., Blum R. D., Quinn D. E., Sellgren K., Whittet D. C. B., 2002, MNRAS, 330, 837
Tonry J. L., et al., 2018, ApJ, 867, 105
Vaillancourt J. E., 2006, PASP, 118, 1340
Vaillancourt J. E., Andersson B.-G., Clemens D. P., Piirola V., Hoang T., Becklin E. E., Caputo M., 2020, ApJ, 905, 157 (V20)
Walker A., Zealey W. J., 1998, Publications of the Astronomical Society of Australia, 15, 79
Whittet D. C. B., 1992, Dust in the galactic environment. Dust in the galactic environment Institute of Physics Publishing, 306 p., http://adsabs.harvard.edu/cgi-bin/nph-bib_query?bibcode=1992QB791.W45.....&db_key=AST
Whittet D. C. B., 2003, Dust in the galactic environment - 2:nd ed.. Dust in the galactic environment Institute of Physics Publishing, 390 p., http://adsabs.harvard.edu/cgi-bin/nph-bib_query?bibcode=2003QB791.W45.....&db_key=AST
Whittet D. C. B., van Breda I. G., 1978, A&A, 66, 57
Whittet D. C. B., Gerakines P. A., Hough J. H., Shenoy S. S., 2001, ApJ, 547, 872
Wilking B. A., Lebofsky M. J., Rieke G. H., 1982, AJ, 87, 695
Ysard N., et al., 2013, A&A, 559, A133
de Geus E. J., 1992, A&A, 262, 258

APPENDIX A: ORIGIN OF THE POTENTIAL RAYLEIGH SCATTERED LIGHT COMPONENT

As discussed in Sect. 2.2 and 3.3, our polarization data show deviations from the ISM/Serkowski functional form for some stars at the bluest wavelengths, in ~~the amount,~~ polarization fraction and position angle. We have modeled this as a Rayleigh scattering component in our analysis.

Because the observations were taken after Astronomical Twilight, and during low lunar illumination and elevations, the question of where this signal originates is important to address.

Given ideal observations and data reduction, any sky polarization will be removed by the data reduction process. Because of the optical complexity of RSS, the *polSALT* pipeline must correct for a number of instrumental effects which also makes the processing complex. We did not attempt to track these through the pipeline code and so cannot with certainty say what may have caused the blue polarization in the *polSALT* outputs. We reitterate that, for the two stars ([JHR80] D-17 and D-20) that were observed together at two different times, the polarization parameters (with the exception of the P.A. for the former) are within the mutual uncertainties in the pairs. Here we will restrict ourselves to 1) noting possible causes of the effect (beyond instrumental ones) and 2) a brief discussion of its impact on our derived polarization parameters.

We first note that while the S/N values in the polarization of individual spectral bins shortward of ~0.5 μm are mostly low and that some of the "signal" could therefore be random, given the inherent positive-definite bias of polarization data (cf Vaillancourt 2006), the spectral fitting was performed in (q,u) space. Below this wavelength the *polSALT* pipeline also often fails to converge and does not produce a measurement (seen as missing data in Figure 3. However, for ~~several~~ three stars ([JHR80] D-1, D-14, D-20) there are significant and systematic deviations from the Serkowski form between ~ 0.5-0.6 μm with reasonable signal-to-noise.

A further indication that the signal may be real arises from the fact that both of the observations acquired on May 13, 2021, ([JHR80] D-14 and D-20) show detectable "Rayleigh" polarization. While the observer's log indicate "Clear" skies, a review of satellite IR imaging (https://meteologix.com/za/satellite/south-africa - available on a 15 min. sampling) indicates that some clouds were present in the vicinity of the SAAO.

In Table A1 we use the boundary of the Western and Northern Cape provinces (about 30 km south of SAAO) as a proxy for "clouds detectable in the area". Because there are ground features that yield variations in the IR images, we compared the different satellite snapshots to assess whether clouds were present or not (The IR satellite image for 09/06/21, UT=19:45, corresponding to observations of [JHR80] D-17, likely shows only ground features). The image for 04/06/21 is clearly brighter, overall, than for the fully clear nights, although this could be a calibration issue with the satellite data. We've listed this as "diffuse". At the observing time for [JHR80] D-20, clouds are detectable **on** the Western/Norther Cape boundary to the south of SAAO (At transit, the Coalsack is located at a zenith angle of ~ 30° south of the SAAO).

Table A1 ~~shows~~ reveals that the observations ~~showing~~ exhibiting Rayleigh components likely had some cloud cover in the SAAO vicinity. In contrast, the observation of [JHR80] D-19 likely had some cloud cover over the observatory (based on the satellite image), but shows no clear "Rayleigh component". (As noted above, the target 19B was observed together with [JHR80] D-19, offset in the slit). For this observation very few of the spectral bins below ~ 0.5 μm converged in the *polSALT* processing.

While we cannot conclusively determine that these spectral fea-

tures are due to atmospheric scattering, there are thus indications that they may be related to the presence of [cirrus] clouds. It is, however and in addition, not clear, given the low elevation of both the Sun and Moon at these observations (and the low Lunar illumination), where the light causing the purported Rayleigh scattering would have originated.

The effects - and local deviation from the Serkowski form - are, still quite clear, especially in the cases of [JHR80] D-1 and D-20. We compared the results of our combined (Serkowski + Rayleigh) fits over the full available spectral range, to fits of only a Serkowski function restricted to λ >0.6 μm. The derived parameters (p_{max} and λ_{max}) are - with the exception of [JHR80] D-20 - within their mutual uncertainties, between the two processees. However, because λ_{max} is usually close to λ=0.6 μm, we have chosen to include the full available wavelength range and therefore the Rayleigh term in our fits.

This paper has been typeset from a TEX/LATEX file prepared by the author.

Table A1. SALT/RSS Observations Data

Star	Date [dd/mm/yy]	Obs. Time (UT)[a] [hh:mm]	Solar El. [°]	Lunar El. [°]	Lunar Illum. [%]	Clouds?	Rayleigh Comp.?
[JHR80] D-1	04/06/21	19:53	-53	-55	25	Diffuse	Yes
[JHR80] D-4	09/05/21	18:11	-30	-42	3	No	No
[JHR80] D-6	08/05/21	19:47	-50	-58	7	No	No
[JHR80] D-14	13/05/21	18:11	-30	-15	4	Yes	Yes
[JHR80] D-17	09/06/21	19:50	-52	-59	0	No	No
[JHR80] D-19	08/05/21	20:41	-61	-61	7	Yes	No
D-19B	08/05/21	20:41	-61	-61	7	Yes	No
[JHR80] D-20	13/05/21	18:52	-38	-23	4	Marginal	Yes

a: Start of observation